

JGR Oceans

RESEARCH ARTICLE

10.1029/2023JC020509

Key Points:

- A representation of internal wave modes that includes dissipation is derived that explains spectra in a tidally forced numerical simulation
- Eliminating the background component of KPP leads to a representation of the physics of internal wave breaking
- Realistic diapycnal diffusivity profiles can be obtained by minor adjustments to the shear component of KPP

Supporting Information:

Supporting Information may be found in the online version of this article.

Correspondence to:

K. Momeni, kayhan.momeni@mail.utoronto.ca

Citation:

Momeni, K., Ma, Y., Peltier, W. R., Menemenlis, D., Thakur, R., Pan, Y., et al. (2024). Breaking Internal waves and ocean diapycnal diffusivity in a high-resolution regional ocean model: Evidence of a waveturbulence cascade. *Journal of Geophysical Research: Oceans*, 129, e2023JC020509. https://doi.org/10.1029/2023JC020509

Received 25 SEP 2023 Accepted 17 MAY 2024

Author Contributions:

Conceptualization: Kayhan Momeni, Yuchen Ma, William R. Peltier, Yulin Pan, Brian K. Arbic

Data curation: Matthew H. Alford Formal analysis: Kayhan Momeni, Yuchen Ma, William R. Peltier, Yulin Pan Investigation: Kayhan Momeni, William R. Peltier, Ritabrata Thakur, Yulin Pan Methodology: Kayhan Momeni, Yuchen Ma, William R. Peltier, Dimitris Menemenlis, Yulin Pan, Brian K. Arbic

© 2024. The Author(s).

This is an open access article under the terms of the Creative Commons
Attribution-NonCommercial-NoDerivs
License, which permits use and distribution in any medium, provided the original work is properly cited, the use is non-commercial and no modifications or adaptations are made.

Breaking Internal Waves and Ocean Diapycnal Diffusivity in a High-Resolution Regional Ocean Model: Evidence of a Wave-Turbulence Cascade

Kayhan Momeni¹, Yuchen Ma¹, William R. Peltier¹, Dimitris Menemenlis², Ritabrata Thakur³, Yulin Pan⁴, Brian K. Arbic³, Joseph Skitka³, and Matthew H. Alford⁵

¹Department of Physics, University of Toronto, Toronto, ON, Canada, ²Jet Propulsion Laboratory, California Institute of Technology, Pasadena, CA, USA, ³Department of Earth and Environmental Sciences, University of Michigan, Ann Arbor, MI, USA, ⁴Department of Naval Architecture and Marine Engineering, University of Michigan, Ann Arbor, MI, USA, ⁵Scripps Institution of Oceanography, University of California San Diego, CA, USA

Abstract It is generally understood that the origin of ocean diapycnal diffusivity is primarily associated with the stratified turbulence produced by breaking internal (gravity) waves (IW). However, it requires significant effort to verify diffusivity values in ocean general circulation models in any particular geographical region of the ocean due to the scarcity of microstructure measurements. Recent analyses of downscaled IW fields from an internal-wave-admitting global ocean simulation into higher-resolution regional configurations northwest of Hawaii have demonstrated a much-improved fit of the simulated IW spectra to the in-situ profiler measurements such as the Garrett-Munk (GM) spectrum. Here, we employ this dynamically downscaled ocean simulation to directly analyze the nature of the IW-breaking and the wave-turbulence cascade in this region. We employ a modified version of the Kappa Profile Parameterization (KPP) to infer what the horizontally averaged vertical profile of diapycnal diffusivity should be, and compare this to the background profile that would be employed in the ocean component of a low-resolution coupled climate model such as the Community Earth System Model (CESM) of the US National Center for Atmospheric Research (NCAR). In pursuing this goal, we also demonstrate that the wavefield in the high-resolution regional domain is dominated by a well-resolved spectrum of low-mode IWs that are predictable by solving an appropriate eigenvalue problem for stratified flow. We finally suggest a new tentative approach to improve the KPP parameterization.

Plain Language Summary A much-improved spectrum of the simulated internal wave (IW) field has recently been obtained by downscaling a global ocean model into a higher-resolution regional configuration. The global simulation is based on the Massachusetts Institute of Technology general circulation model (MITgcm) forced by both astronomical tidal potential and surface atmospheric processes. By employing a mathematical framework to predict the structure of IWs, we first demonstrate that the interior wavefield of the high-resolution regional domain is well dominated by a series of low-order IW modes. Then, we address the issue as to whether the component of the K-Profile Parameterization (KPP) associated with IW shear might be able to explain the physical origins of the background depth dependence of diapycnal diffusivity that would normally be employed in the ocean component of a modern coupled climate model. Finally, we suggest a tentative approach to further improve KPP.

1. Introduction

Numerical ocean modeling has experienced great improvements in recent years due to the advance in computational power; until recently, researchers had been focusing more strongly on the atmospheric component of the climate system. It is unsurprising because the energized scales of atmospheric motions are an order of magnitude larger than those of the oceans. However, in the oceanic context, it is crucial to consider not only the scales of geostrophic motions but also the presence of submesoscale oceanic frontal structures. Additionally, the volume-filling field of internal (gravity) waves (IW) plays a vital role, being excited by the interaction of the barotropic tide with bottom topography and surface wind forcing. Therefore, current ocean models have made significant advancements in various aspects, including the utilization of concurrent "wind plus tides" forcing. These models are demonstrating remarkable progress in terms of resolution, bathymetric maps, and parameterization schemes. Today, direct access to such small scales will require us to begin with high-resolution results for global

MOMENI ET AL. 1 of 23

Software: Kayhan Momeni, Dimitris Menemenlis, Ritabrata Thakur, Yulin Pan

Supervision: William R. Peltier Validation: Kayhan Momeni, William R. Peltier, Yulin Pan, Brian K. Arbic, Joseph Skitka

Visualization: Kayhan Momeni, Ritabrata Thakur

Writing - original draft:

Kayhan Momeni, Yuchen Ma, William R. Peltier, Dimitris Menemenlis, Ritabrata Thakur, Yulin Pan, Brian K. Arbic, Joseph Skitka, Matthew H. Alford

Writing – review & editing: Kayhan Momeni, Yuchen Ma, William R. Peltier, Dimitris Menemenlis, Ritabrata Thakur, Yulin Pan, Brian K. Arbic simulations of the kind described in Arbic et al. (2018) but also to dynamically downscale the results of such models into an even higher resolution regional domain.

Two of the most prominent examples (Arbic et al., 2018) of such astronomically and atmospherically forced global simulations are the US Navy runs of the HYbrid Coordinate Ocean Model, *HYCOM* (Bleck, 2002), and the NASA simulations of the Massachusetts Institute of Technology general circulation model, *MITgcm* (Marshall et al., 1997). The HYCOM wind plus tides global models are typically run with horizontal grid spacings of 1/12.5° and 1/25°. HYCOM simulations have been more extensively vetted with observations than their MITgcm counterparts. However, the MITgcm-based global wind plus tides simulations have been run with higher resolution, in particular with 90 depth levels and with horizontal grid spacings of 1/12°, 1/24°, and 1/48°. In its highest resolution incarnation, the latter model (referred to below as *MITgcm48* or *LLC4320*) will play a prominent role in our discussion of ocean turbulent diapycnal diffusivity.

Although global models that include both tidal and atmospheric forcing have been employed for a long time (e.g., in Thomas et al. (2001) and Schiller and Fiedler (2007)), it has been only relatively recently that they have been run with fine horizontal grid spacings (1/12° or less). Müller et al. (2015), based upon HYCOM results, observed that high-resolution global models with simultaneous tidal and atmospheric forcing had produced a quasi-realistic IW spectrum. Furthermore, they concluded that as the model resolution increased, the frequency and wavenumber spectra approached observations and theoretical expectations. Further work of Rocha et al. (2016) used the MITgcm48 simulations and showed that MITgcm-based models also possess a partial IW spectrum. In fact, Savage et al. (2017) compared model spectra with those derived from data collected on *McLane Moored Profiler* (MMP), as well as the empirical Garrett-Munk (GM) spectrum of Cairns and Williams (1976). They concluded that MITgcm48 has a closer spectral continuum of IWs to observations and therefore is preferable over HYCOM25 for global IW modeling in cases where a filled-out spectrum rather than internal tide accuracy is the primary concern.

Internal waves owe their existence in the ocean to stable density stratification: a parcel of fluid that is adiabatically displaced in the vertical direction will be subjected to a buoyant restoring force that will act to return it to its original position. The frequency with which a vertically displaced parcel oscillates around its original position is called the buoyancy frequency, denoted N, and is such that its square is proportional to the strength of the vertical density gradient (i.e., when considering z to be increasing downward, $N^2 = \frac{g}{\rho} \frac{\partial p}{\partial z}$.) The existence of stable density stratification enables the existence of a family of freely propagating plane IWs. In a region of the oceans in which the local vertical component of Earth's angular velocity of rotation is given by the Coriolis parameter f, and N is fixed, the dispersion relation of these plane waves is:

$$\omega^2 = \frac{m^2 f^2 + N^2 (k^2 + l^2)}{m^2 + (k^2 + l^2)},\tag{1}$$

in which ω is the temporal frequency, f is also referred to as the inertial frequency, and k, l, and m are zonal, meridional, and vertical wavenumbers, respectively. Introducing a change of variables of $\sin^2(\theta) \equiv \frac{m^2}{k^2 + l^2 + m^2}$, Equation 1 can be re-expressed as follows:

$$\omega^2 = N^2 \cos^2(\theta) + f^2 \sin^2(\theta). \tag{2}$$

According to Equation 2, the permissible range for the IWs' frequency ω is such that $f \le \omega \le N$. However, it is important to understand that the dispersion relation (1) is for fully non-hydrostatic plane waves. In contrast, the MITgcm model used in this study is run in the hydrostatic mode. The dispersion relation in the hydrostatic regime is as follows:

$$\omega^2 = N^2 \frac{k^2 + l^2}{m^2} + f^2,\tag{3}$$

Although the hydrostatic dispersion relation allows propagation to persist for all frequencies $\omega > f$, for sufficiently high frequency, the hydrostatic assumption $m^2 \gg k^2 + l^2$ would itself be violated.

MOMENI ET AL. 2 of 23

LLC4320 is a forward simulation, the results from which is employed herein to force an even higher resolution regional model that was run in the hydrostatic configuration. LLC4320 is run with a nominal 1/48° horizontal grid spacing and 90 vertical levels. The horizontal grid spacing is equivalent to ~2.3 km near the equator and much less at high latitudes. The thickness of the vertical level spacing increases from 1 m at the surface to 480 m near the 7 km depth level. This internal-wave-admitting global ocean simulation was forced by six-hourly updates of the atmospheric wind, pressure, and buoyancy fields, taken from the European Center for Medium-Range Weather Forecasts (ECMWF), that are applied to the ocean surface. The astronomical tidal potential with which the model is forced employs the full lunisolar potential based on the solution provided in Ponte et al. (2015). The global LLC4320 simulation includes interactive sea ice in the polar oceans, as per Losch et al. (2010). Of particular importance to the work described herein is that the background vertical mixing values of LLC4320 were set based on the Arctic Ocean optimization of Nguyen et al. (2011). As will be discussed, this Arctic-Ocean-centric choice of background mixing coefficients has some unintended consequences for diapycnal mixing in the global simulation.

A further significant advance in the ability of ocean models forced by both tides and atmospheric fields to accurately capture a fully realistic internal gravity wave spectrum was recently achieved in the work of Nelson et al. (2020). They employed the available LLC4320 simulation and chose a specific period of time and a confined regional domain to the northwest of Hawaii as a target for analysis of the IW field. The regional domain was bounded by 24°-32°N, 193°-199°E in the North Pacific Ocean, and is shown in Figure 1. The time window was particularly chosen to include the season during which MMP observations were made within the region of interest, though not during the same year. Furthermore, the location of the regional domain was also chosen to encompass the region where a set of four MMP profilers had been deployed (Alford et al., 2007). These profilers were deployed to measure the IW spectrum at a series of locations in the North Pacific Ocean, along the track of IW beams coming from the Hawaiian Islands (Figure 1 illustrates the variation of bathymetric depth along the path of the internal wave beam as well as the positioning of the profilers along this path.) Nelson et al. (2020) dynamically downscaled LLC4320 to a much finer grid spacing of 250 m in the horizontal and 270 vertical levels. The same tidal and atmospheric forcing fields as those in LLC4320 and hard boundary conditions at the lateral boundaries were applied (i.e., the model variables at the lateral boundaries were forced to be equal to the hourly outputs of LLC4320.) The downscaling method employed no complex data assimilation methods to eliminate boundary reflections such as those that might be minimized by employing a "sponge" as has often been found to be useful for the dynamical downscaling of global atmospheric or oceanic dynamical applications (e.g., see Gula and Peltier (2012); Siyanbola et al. (2023)). Nevertheless, the analyzed high-resolution data sets were not strongly contaminated by the "hard" data assimilation method employed for ingesting global model forcing. The most important results reported in Nelson et al. (2020) consisted first of the demonstration that the high-resolution hydrodynamic fluctuations being produced in the regional domain were, indeed, of the form expected if these fluctuations were IWs. This was established by exploiting the consistency relations between the hydrodynamic fields that are characteristic of IWs. The second contribution of that paper involved comparing the spectral characteristics of the IW-related fluctuations with expectations based upon these characteristics of the empirical spectrum of Garrett and Munk (Cairns & Williams, 1976) and the profiler measurements.

Empirical identification of the GM spectrum of IWs has been one of the most significant contributions to physical oceanography in the past 50 years, which relates the IW energy to its associated temporal frequency ω and vertical wavenumber m distribution (Garrett & Munk, 1971, 1972, 1975). The revision by Cairns and Williams (1976) is called the GM76 spectrum. This model assumes that spectral energy density is a separable function of ω and m. For sufficiently large wavenumbers, the energy density can be written as:

$$E(\omega, m) = E_0 G(\omega) H(m), \tag{4}$$

where $G(\omega)$ and H(m) have the following properties:

$$G(\omega) \propto f\omega^{-1} (\omega^2 - f^2)^{-1/2}, \qquad H(m) \propto (m^2 + m_*^2)^{-1}.$$
 (5)

and m* is a fixed reference vertical wavenumber. The normalization properties $f_f^N G(\omega) d\omega = 1$ and $\int_0^\infty H(m) dm = 1$ are held. From Equation 5, it is implied that the energy density for sufficiently high vertical wave

MOMENI ET AL. 3 of 23

21699291, 2024, 6, Downloaded from https://agupubs.onlinelibrary.wiley.com/doi/10.1029/2023IC020509, Wiley Online Library on [21/02/2025] See the Terms and Conditions (https://onlinelibrary.wiley.com/dems-and-conditions) on Wiley Online Library for rules of use; OA articles are governed by the applicable Creative Commons Licensia.

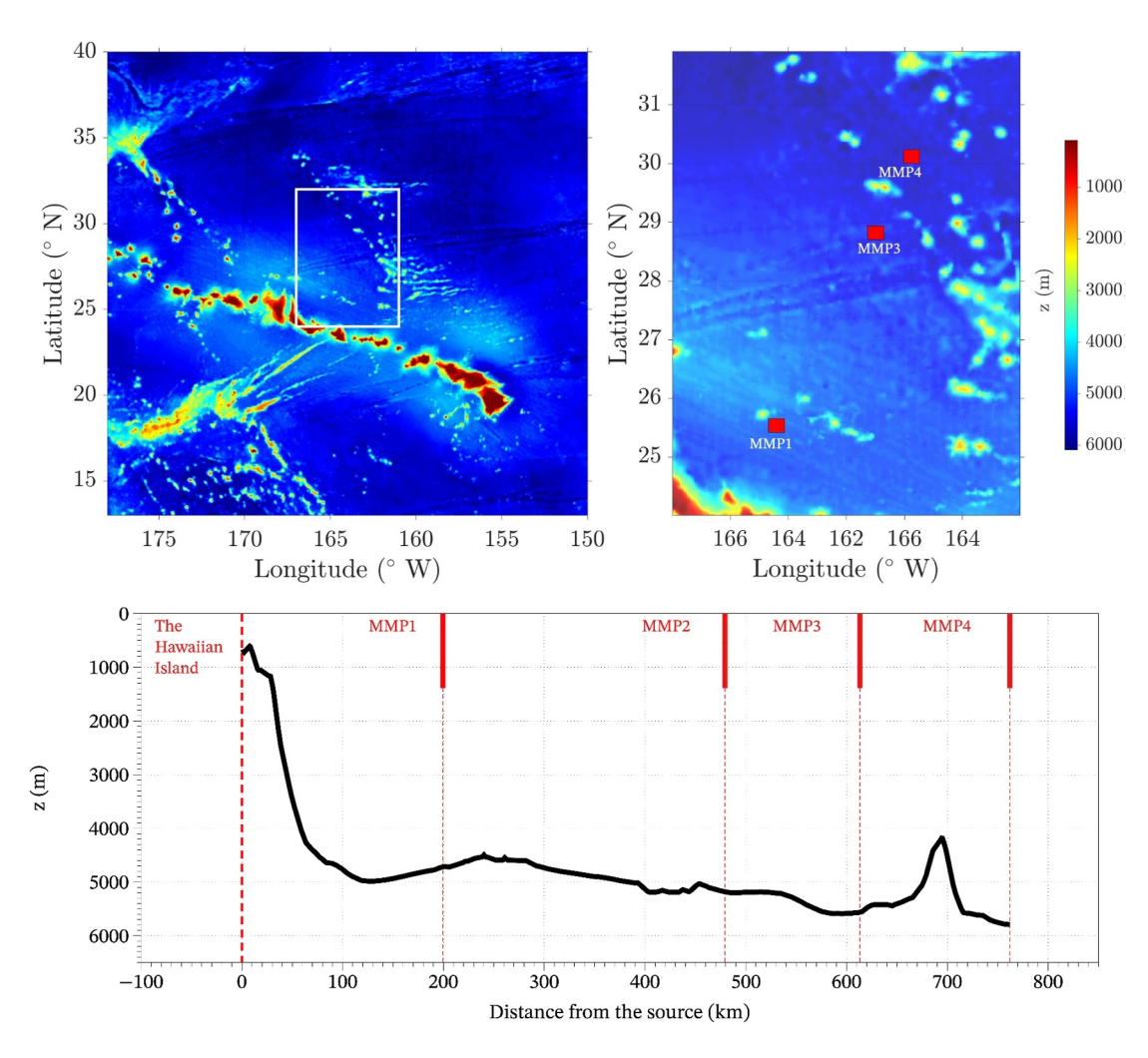


Figure 1. The top-left panel displays the Northeast Pacific basin, highlighting the study area through the use of a white rectangle. The top-right panel provides an enlarged perspective of the simulation domain, featuring the positions of the McLane moored profilers (MMP1, MMP3, and MMP4) as collected by Alford et al. (2007), represented by red solid blocks. The bottom panel illustrates the bathymetry along the trajectory of the IW beams.

numbers and temporal frequencies should follow $E(\omega) \propto \omega^{-2}$ and $E(m) \propto m^{-2}$, which implies that the continuum should have a power law form with the power law exponent of -2.

Although the analysis of high resolution dynamically downscaled LLC4320 data in Nelson et al. (2020) confirmed that the horizontal wavenumber and temporal frequency spectra of kinetic energy were in accord with the predictions of GM76, the vertical wave number spectrum was found to deviate significantly from the GM76 predictions. Pan et al. (2020) used this high-resolution regional model and computed the power spectrum of the horizontal wavenumber $K \equiv \sqrt{k^2 + l^2}$ and temporal frequency ω on a single vertical level at a depth of z = 500 m. They showed that spectral power is concentrated along a series of dispersion curves that extend from the inertial frequency f with a positive slope in the $K - \omega$ space. Although up to five IW modes of the ocean waveguide are represented in the high-resolution regional domain, none of the expected higher-order modes are similarly well defined. These high-order modes are critical because the lack of energy in the high-mode region causes the significant deviation of the vertical wavenumber spectrum from the one predicted in the GM76 model captured in Nelson et al. (2020). In a later work, Thakur et al. (2022) exploited the same regional setup, albeit with lower horizontal resolutions typical of the global model, and compared the IW continuum of the model with that of observations. They demonstrated that in ocean models where IWs have begun to be resolved, the background component of the *Kappa-Profile-Parameterization (KPP)* must be turned off to maintain the proper spectral level

MOMENI ET AL. 4 of 23

of IWs. One of the most important contributions of the present paper will be to explain the reason for this discrepancy between GM76 and the numerically captured vertical wavenumber spectrum. As we will discuss in detail in what follows, the explanation for this misfit will be found in a peculiarity of the parameterization of ocean diapycnal diffusivity employed in the design of the global LLC4320. The present paper also explains the reason behind the improvement in the vertical wavenumber spectrum achieved in Thakur et al. (2022).

Mixing occurs due to various phenomena with over 20 different physical origins (Garrett, 2003) and breaking IWs are considered the primary source of turbulent diapycnal mixing away from surface and bottom boundary layers (MacKinnon et al., 2017). Therefore, understanding the physical origins and efficacy of mixing phenomena is crucial. For example, Alford and Pinkel (2000) measured over two thousand such mixing events in the thermocline and mapped them relative to various fields, enabling them to illustrate different classes of such mixing events. Mixing associated with IWs and IW-breaking has also been recently reviewed in MacKinnon et al. (2017). Because the turbulent mixing is not resolvable in the grid cells of our numerical model, an effective parameterization must be employed. However, the high intermittency of turbulent mixing makes it extremely difficult to measure effective diapycnal mixing observationally. In fact, Baker and Gibson (1987) argue that since the distribution of the dissipation rate is log-normal, the fat-tail of the distribution might cause an underestimation in observational measurements of diapycnal mixing.

Parameterization schemes for diapycnal mixing have been evolving over time, from a uniform constant space-time value to a depth-dependent function (Bryan & Lewis, 1979), to models that separate the surface boundary layer, which is controlled mostly by buoyancy inputs and wind, from interior processes that are controlled mostly by convection, shear, and double-diffusive processes (Gaspar et al., 1990; Large et al., 1994; Pacanowski & Philander, 1981). Today, the most widely used parameterizations for diapycnal mixing are the KPP scheme (Large et al., 1994), the *Mellor-Yamada* 2.5 level turbulence closure (Mellor & Yamada, 1982), and the *Generic Length Scale (GLS)* scheme (Umlauf & Burchard, 2003). An overview of the evolution of such schemes is discussed in detail in the supporting information of Peltier and Vettoretti (2014).

LLC4320 uses a modified KPP scheme to model subgrid-scale turbulence. KPP consists of two separate representations: one- internal mixing and 2- boundary layer mixing. A threshold of 0.3 for the bulk Richardson number determines the depth of the mixed layer upon which the boundary layer mixing scheme acts. On the other hand, the interior ocean is controlled by the internal mixing scheme of KPP that consists of three components, each representing a different physical mixing phenomenon. The effective diapycnal diffusivity and turbulent momentum diffusivity in the interior ocean is assumed to be a linear superposition of these components:

$$\kappa = \kappa_W + \kappa_S + \kappa_C, \qquad \nu = \nu_W + \nu_S + \nu_C, \tag{6}$$

where "W" denotes the background mixing component that is taken to be a function of depth only and fixed for all basins of the global ocean, "S" denotes the shear instability component and is taken to be a function of Richardson number $Ri = \frac{g}{\rho} \frac{\partial \rho/\partial z}{(\partial u/\partial z)^2}$, and "C" denotes the convective destabilization component, which is activated only when the fluid becomes statically unstable (Ri < 0.) In this case, streamlines are "overturned", and the local vertical density gradient is positive, so the mixing is extremely intense. In the original KPP model of Large et al. (1994), another term exists that represents mixing due to the action of double diffusion processes that operate in circumstances where the differences between the molecular diffusivities of heat and salt play an important role. Although this difference might be important in regions in which thermohaline staircase structures form (e.g., see Peltier et al. (2020)), in the analyses to be discussed herein, such doubly diffusive influence will play no significant role and is not considered in the numerical model as well.

The background and the shear components are the most important aspects of this mixing parameterization in the present context. The background component of KPP is a crude parameterization of the mean effective depth-dependent turbulent value for viscosity and diffusivity. In Figure 2, we compare the peculiar background component used in LLC4320, which is based on the Arctic optimization of Nguyen et al. (2011), with the same component of a "standard KPP". By the background component of a "standard KPP" we mean the form of background viscosity and diffusivity that are often assumed in a typical low-resolution ocean component of a coupled climate model to simulate global warming and climate change processes, in this case, the University of

MOMENI ET AL. 5 of 23

conditions) on Wiley Online Library for rules of use; OA articles are governed by the applicable Creative Commons Licens

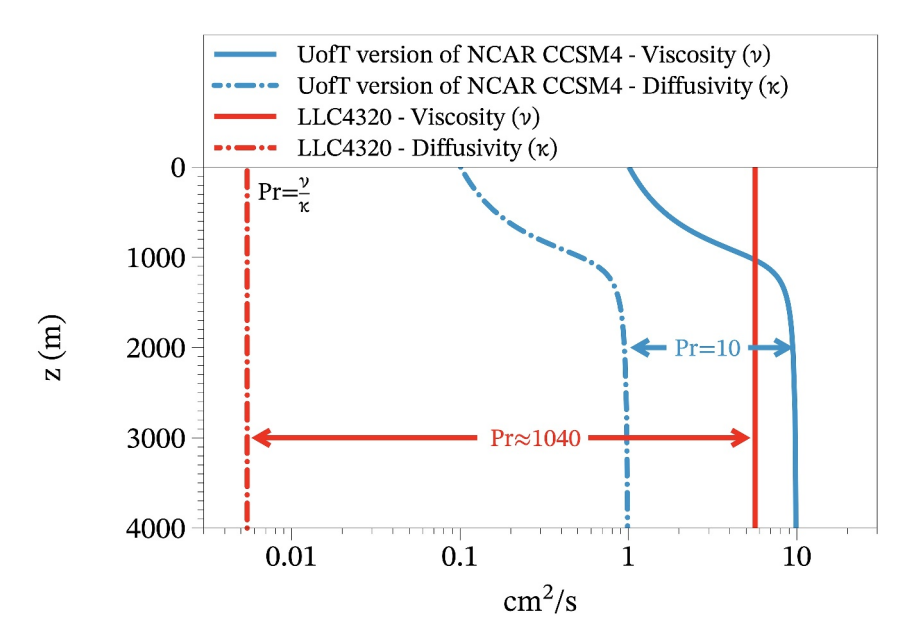


Figure 2. Comparison of the University of Toronto version of the NCAR CCSM4 depth-dependent background component of KPP and the one employed in LLC4320. Also shown on the figure is the fundamental difference between the Prandtl number associated with these two different versions of the KPP background, which will play an important role in the discussion to follow in this paper.

Toronto version of the *NCAR CCSM4* model, a structure referred to in the literature as *UofT CCSM4* (see Peltier & Vettoretti, 2014, for a description). This background component has the following form (note that z is in meters):

$$\kappa_W(z) = 0.524 + 0.313 \tan^{-1} \left(\frac{z - 1000}{222.2} \right) \text{cm}^2 / \text{s}, \qquad \nu_W(z) = 10 \kappa_W(z).$$
(7)

The most important property of this background is that in the deep ocean below the main thermocline, the diapycnal diffusivity is equal to the value of 1 cm²/s, which Munk (1966) first demonstrated is required to enable the deep water that forms by convective instability in the polar regions to return to the surface so as to complete the global overturning circulation.

Notable is the fact that in the high-resolution LLC4320 global model, the diapycnal diffusivity has been almost entirely eliminated from the background component of KPP, and the ratio of background viscosity to diffusivity (i.e., the Prandtl number Pr) is $Pr \approx 1,040$. The small constant value of diapycnal diffusivity (5.4 × 10–3 cm²/s) in the global LLC4320 simulation enabled maintenance of the Arctic halocline (Nguyen et al., 2009) while the optimized diapycnal viscosity (5.7 cm²/s) has a more traditional value (Nguyen et al., 2011). As we will show in what follows, this high value of the Prandtl number inhibits the parameterized breaking of IWs in LLC4320. Therefore, turning off this background component will play a critical role in the analyses of IW breaking, which will be discussed in detail in Section 3 to follow.

We are interested in employing high-resolution regional model simulations to better understand the connection between the parameterized breaking of IWs and the diapycnal diffusivity in the ocean models. Although we expect this turbulent diffusivity to be a strong function of longitude and latitude, we also expect that its magnitude in the abyssal ocean should be near 1 cm²/s (Munk, 1966). We intend to employ the background component of the NCAR CCSM4 model with such magnitude in the abyssal ocean and compare it with the diapycnal diffusivity profiles we can predict based on our IW-breaking model.

The importance of obtaining accurate vertical profiles of ocean diapycnal diffusivity throughout the oceans has been made abundantly clear based on the recognition of the so-called "pattern effect" upon climate model sensitivity (Andrews et al., 2018; Dong et al., 2019). This effect is such that if climate sensitivity is determined on the basis of models that have sea surface temperature (SST) patterns fixed to those observed, then the models are

MOMENI ET AL. 6 of 23

characterized by relatively low climate sensitivity. In contrast, free-running coupled atmosphere-ocean models that deliver SST patterns discordant with observation are characterized by high climate sensitivity. Note that ocean mixing processes, including turbulent diapycnal diffusivity, are known to provide highly significant controls upon the SST field.

The analyses presented in this paper aim to investigate whether the weak damping of the IW field, forced by both tides and winds, allows for a realistic IW spectrum within the high-resolution regional domain. Additionally, a crucial aspect under examination is whether this spectrum will support a depth dependence of diapycnal diffusivity. This dependence arises from IW breaking, as represented by the shear component of the KPP parameterization. Notably, our study modifies this parameterization to a form applicable for describing turbulence resulting from IW breaking. In Section 2 of the paper to follow, we will address the quality of the internal tidal component of the field of IWs in the high-resolution regional domain and the ability of a mathematical model to accurately predict the observed modes of the stratified ocean waveguide. In Section 3 of the paper, we investigate the ability to map the IW-breaking process into a depth dependence of diapycnal diffusivity that reasonably approximates that characteristic of the UofT CCSM4 global climate model. Conclusions that follow from these analyses are offered in Section 4.

2. Internal Waves in the High-Resolution Regional Domain: Simulations and Theoretical Predictions

Because the LLC4320 simulation includes the influence of both wind forcing and tidal forcing as described by the full astronomical potential and because it also includes an acceptably accurate representation of ocean floor topography, the ocean response to forcings is expected to include a full spectrum of the IWs excited by this interaction. Because a huge Prandtl number in the background component of KPP is employed, these waves are inhibited from breaking. If measured in the far field of their excitation sources, these IWs should consist of a discrete set of the normal modes of the density-stratified ocean waveguide. In Section 2.1, we will discuss the extent to which the high-resolution regional ocean model is able to resolve these modal structures. Section 2.2 will investigate the extent to which the observed spectrum is mathematically predictable.

2.1. Energy Spectrum of Internal Waves in the High-Resolution Regional Simulation

We examine the energy spectrum in the horizontal wavenumber K - temporal frequency ω space at a single vertical level, in order to identify the modal structure of IWs discussed above. For the present paper, we will use the high-resolution dynamically downscaled simulation used by Nelson et al. (2020) and Pan et al. (2020), as well as another high-resolution dynamically downscaled simulation in which, all aspects are similar to the previous simulation except that, following Thakur et al. (2022)'s results, the background component of KPP is turned off. Note that the background component of KPP is turned on in the global model; it is only in the high-resolution regional domain that we have control over this parameter. The resulting spectra are presented in Figure 3.

Panel (a) of Figure 3 displays the energy spectrum in the $K-\omega$ space for the original simulation of Nelson et al. (2020) over a single vertical level (z = 500 m). Although it is based on the simulation of Nelson et al. (2020), the spectrum was not shown there and rather was originally computed and shown in Pan et al. (2020) (see their Figure 8) Panel (b) of Figure 3 displays the same computation for the new simulation with the background component of KPP turned off. Comparing these two panels, one observes that turning off the background component of KPP results in more energy accumulation in the high-mode (upper-left hand) region of the $K-\omega$ space. As we will see in the following section of this paper, this small difference will be of fundamental importance in all that follows. Panel (c) of Figure 3 displays the spectrum of the sea surface height squared SSH2 in the $K-\omega$ space for the simulation with the KPP background turned on. Panel (d) displays the same spectra for the new simulation with the KPP background turned off. Harmonics of the atmospheric update frequency (i.e., 6-hourly updates) are evident as energetic vertical lines on both bottom SSH2 panels. Evident in all panels is the onset of aliasing in the lowest order modes beyond a certain frequency, which is apparent as reflection at the right boundary. That aliasing is a consequence of the fact that the highest frequency in the plot is in fact the Nyquist frequency beyond which all energy is folded back to lower frequency. Figure 3 clearly demonstrates the presence of IW modes both in the sea surface height and the interior ocean. Although the largescale SSH field variability is primarily controlled by prescribed water mass fluxes at the lateral boundaries of the

MOMENI ET AL. 7 of 23

21699291, 2024, 6, Downloaded from https://agupubs.onlinelibrary.wiley.com/doi/10.1029/2023IC020509, Wiley Online Library on [21/02/2025]. See the Terms and Conditions (https://onlinelibrary.wiley

ons) on Wiley Online Library for rules of use; OA articles are governed by the applicable Creative Commons Licenso

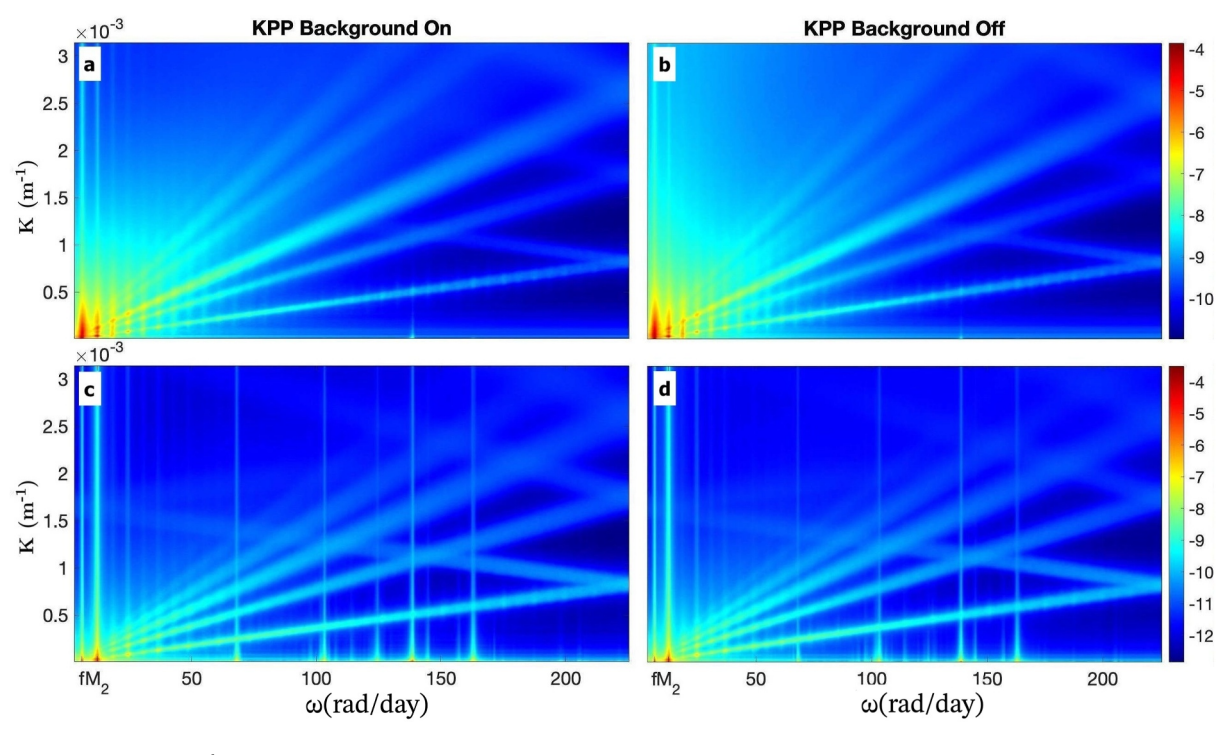


Figure 3. Kinetic energy spectrum $E^k(K,\omega)$ of the dynamically downscaled model in the horizontal wavenumber-temporal frequency $(K-\omega)$ space. The top row shows $\log_{10}E^k(K,\omega)$ (m³ day s⁻² rad⁻¹) evaluated at z=500 m. The bottom row shows the spectrum of sea surface height squared SSH2 (m³ day rad⁻¹) for the same time and period. The left column shows the spectra for the same high-resolution simulation as Nelson et al. (2020). The right column shows the spectra for the new simulation with the background KPP turned off.

regional domain, the smaller scales are an expression of local submesoscale and internal wave activity, which can differ from that of the global LLC4320 simulation in the same region. This is of special importance, particularly after the launch of the Surface Water and Ocean Topography (SWOT) mission, which will provide researchers with high-resolution SSH data. As the plot suggests, the SSH data is dominated by the presence of IW in the interior ocean, which must be filtered out for other analyses, including analyses of mesoscale eddies. Furthermore, analyses of this kind could relate the interior mixing phenomena with surface signatures that are easier to observe.

In Section 3.1 below, a detailed explanation of this observed difference between the KPP background on and the KPP background off cases for the internal wave spectrum will be provided. This explanation will play an important role in our discussion to follow. In order to understand these differences, first a mathematical framework for the theoretical study of all modes will be introduced in Section 2.2 below.

2.2. Mathematical Predictability of the Internal Wave Modes

In this subsection, we will use a Galerkin-method-based approach to calculate the modal lines and analyze the damping of each mode caused by the prescribed diffusivity and viscosity. While Equation 1 defines the plane wave dispersion relation, the underlying assumption is that the vertical wavenumber m can take on any real value. This is not valid in reality if the full ocean depth is considered as a waveguide; In the ocean with full depth L, the vertical wavenumber m can only take discrete values $m_j = \frac{2\pi j}{L}$ as shown in the discrete modal structure captured in Figure 3. To study the system under this realistic condition, we begin by writing the Reynolds-averaged Navier-Stokes (RANS) equations for continuity, momentum, and energy conservation under the turbulent viscosity and gradient diffusion hypothesis:

MOMENI ET AL. 8 of 23

21699291, 2024, 6, Downloaded from https://agupubs.onlinelibrary.wiley.com/doi/10.1029/2023JC020509, Wiley Online Library on [21/02/2025]. See the Terms and Conditions

$$u_{x} + v_{y} + w_{z} = 0$$

$$u_{t} + uu_{x} + vu_{y} + wu_{z} = -\frac{p_{x}}{\rho_{0}} + \nu \nabla^{2} u + fv$$

$$v_{t} + uv_{x} + vv_{y} + wv_{z} = -\frac{p_{y}}{\rho_{0}} + \nu \nabla^{2} v - fu$$

$$w_{t} + uw_{x} + vw_{y} + ww_{z} = -\frac{p_{z}}{\rho_{0}} + \nu \nabla^{2} w - g \frac{\rho}{\rho_{0}}$$

$$\rho_{t} + u\rho_{x} + v\rho_{y} + w\rho_{z} = \kappa \nabla^{2} \rho$$
(8)

These equations represent the long-term mean characteristics of the system over a large ensemble of realizations of turbulent flow conditions. Note that κ and ν represent the effective diffusivity and viscosity, respectively, that are induced by smaller-scale turbulent phenomena. They are usually much larger than molecular diffusivity and viscosity. Following the standard procedure, we decompose each field into background constant and wave-like perturbation terms. The perturbation terms are considered to be as follows:

$$\left\{u',v',w',p',\rho'\right\}(x,y,z,t) = \left\{\tilde{u}(z),\tilde{v}(z),\tilde{w}(z),\tilde{p}(z),\tilde{\rho}(z)\right\}e^{(\sigma t - i(kx + ly))},\tag{9}$$

where

$$\{\tilde{u}(z), \tilde{v}(z), \tilde{p}(z)\} = \sum_{j=1}^{J} \{u_j, v_j, p_j\} \cos(m_j z),$$

$$\{\tilde{w}(z), \tilde{\rho}(z)\} = \sum_{j=1}^{J} \{w_j, \rho_j\} \sin(m_j z).$$
(10)

The above perturbation terms are written assuming that each term's vertical and horizontal dependence are separable. Besides, the vertical dependencies are projected on a set of orthogonal basis functions. The set of orthogonal basis functions $g_j(z) = \sin(m_j z)$ are chosen in such a way that they satisfy both orthogonality (i.e., $\frac{2}{L} \int_0^L g_i(z)g_j(z)dz = \delta_{ij}$) and the rigid boundary conditions (i.e., $\tilde{w}(0) = \tilde{w}(L) = 0$). Although there is another common way to choose the vertical basis function, which is based on the local stratification (e.g., see Pan et al. (2021)), this simpler way of using sin/cos terms is sufficient for the purpose of representing the IW field from the model.

Moreover, σ is the complex frequency with the imaginary part $\sigma_{im} \equiv \omega$ being the temporal frequency and the real part σ_{re} being modal attenuation/amplification, and J depends on the resolution of the model (i.e., the number of modes in terms of which we truncate the vertical modal series.) By assuming Galerkin projection of Equation 9 and substituting the decomposed form of fields into Equation 8, after neglecting second-order or higher perturbation terms and also neglecting derivatives of κ and ν , we get:

$$\sigma\Omega_{i} = -\nu k_{j}^{2} \Omega_{j} - f m_{i} w_{i},$$

$$\sigma k_{i}^{2} w_{i} = -\nu k_{j}^{2} m_{j}^{2} w_{j} - \nu k_{j}^{2} (k^{2} + l^{2}) w_{j} - \frac{g}{\rho_{0}} (k^{2} + l^{2}) \rho_{i} + f m_{i},$$

$$\sigma\rho_{i} = -\rho_{zij} w_{j} - \kappa k_{i}^{2} \rho_{j},$$
(11)

where $k_j^2 \equiv k^2 + l^2 + m_j^2$, $\Omega_j \equiv ikv_j - ilu_j$, and

$$\rho_{zij} = \frac{2}{L} \int_0^L \sin(m_i z) \sin(m_j z) \frac{\partial \bar{\rho}(z)}{\partial z} dz.$$
 (12)

MOMENI ET AL. 9 of 23

21699291, 2024, 6, Downloaded from https://agupubs.onlinelibrary.wiley.com/doi/10.1029/2023/C020509, Wiley Online Library on [21/02/2025]. See the Terms and Conditions (https://onlinelibrary.wiley.com/term/term)

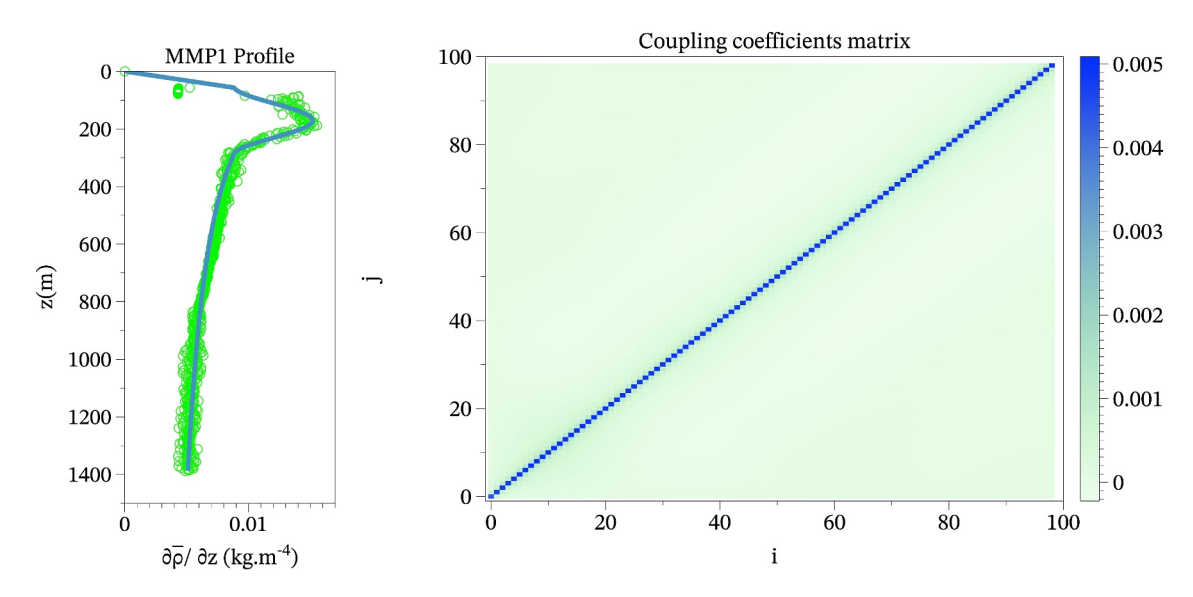


Figure 4. (Left) The profile of observed $\frac{\partial \bar{p}}{\partial z}$ at the MMP1 location (green points). The Solid blue line shows the fitted profile using a hyperbolic tangent hat followed by a cosine bell and a power decay. (Right) The coupling coefficients between the waveguide modes based on Equation 12.

Equation 11 defines an eigenvalue problem. Note that there is a long history of analyses of the internal wave spectrum, based upon the assumption that both κ and ν are zero (Kundu et al., 2015; Lamb, 2014; Wunsch, 1975). Under these assumptions, the above equations reduce to a single equation for velocity:

$$\frac{\partial^2 \tilde{w}(z)}{\partial z^2} + \frac{N^2(z) - \omega^2}{\omega^2 - f^2} (k^2 + l^2) \, \tilde{w}(z) = 0, \tag{13}$$

with the boundary condition $\tilde{w}(0) = \tilde{w}(L) = 0$. In the current study, we include the viscosity and diffusivity terms to investigate the potential influence of these dissipation terms on the IW modes.

To solve this eigenvalue problem, we need to calculate the coupling coefficients between the modes ρ_{zij} . As it is evident from Equation 12, the coupling coefficients require the profile of density gradient $\frac{\partial \bar{p}}{\partial z}$ in the ocean. The profiles of density change for MMP observations are publicly available. However, these profiles need to be continuously integrated over depth. Because the data points are discrete, a reanalysis is performed on the profile data. Figure 4 (left) shows the discrete data points of the stratification profile in green dots at the southernmost MMP location. The reanalysis curve is fitted assuming that the profile of $\frac{\partial \bar{p}}{\partial z}$ is identically zero at the top mixed layers; this can be modeled as a *tanh* function with a sharp transition; then, the *tanh* function is immediately followed by a *cosine* bell; finally, it *exponentially* decays. Following this procedure, the reanalysis curve is superimposed on data points of Figure 4 (left) in the blue line. Using the blue curve of Figure 4 (left) for $\frac{\partial \bar{p}}{\partial z}$, coupling coefficients between the modes can be computed according to Equation 12. Figure 4 (right) shows the computed coupling coefficients for the southern-most MMP observation. Although formally, on the basis of Equation 12, it is entirely plausible that coupling between IW modes should be produced by depth variation of buoyancy frequency, in this particular region of the ocean where the depth dependence of buoyancy frequency is shown in Figure 4 (left), this coupling is so weak that the coefficient matrix in Figure 4 (right) is strongly diagonal and the IW modes are essentially uncoupled from one another.

Using an eigenvalue solver, Equation 11 can be solved to obtain the complex frequency σ at a specific $K^2 \equiv k^2 + l^2$. Figure 5 demonstrates the imaginary part of the results of Equation 11 in the range $K \leq 3 \times 10^{-3} \ m^{-1}$ for three values of water column depth L. Even though the impact of significant changes in the bathymetric depth by 30% has been explored in the three panels of Figure 5, the impact upon the spectrum is relatively small. This is a critical point concerning the expected spectrum of internal waves in the ocean, because variations in bathymetric depth of this kind, away from the regions where the IWs are generated, namely sea mounts and continental shelves which are shallow, are very modest (the bathymetry along the path of IW beam is shown in Figure 1 (bottom)). So

MOMENI ET AL. 10 of 23

21699291, 2024, 6, Downloaded from https://agupubs.onlinelibrary.wiley.com/doi/10.1029/2023JC020509, Wiley Online Library on [21/02/2025]. See the Terms and Conditions (https://onlinelibrary.wiley

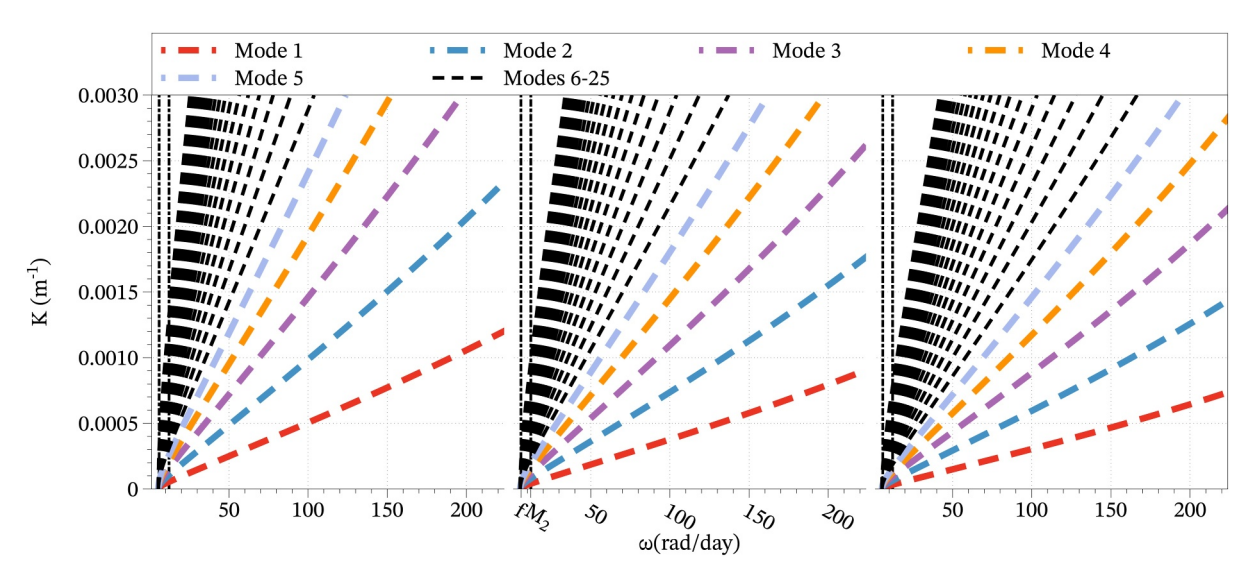


Figure 5. The modal structure of internal gravity waves at the MMP1 location. (Left) demonstrates the solution to the eigenvalue problem according to Equation 11 for the case where the water column depth L is 30% less than the actual value of 4,719 m. (Centre) demonstrates the solution where the water column depth L is exactly the actual value of 4,719 m. (Right) demonstrates the solution where the water column depth L is 30% more than the actual value of 4,719 m.

we are expecting that the variation in the spectrum of IWs measured in the regions away from the regions of generation should be modest as well. Because the GM spectrum is primarily based upon the high-frequency portion of the IW spectrum, it becomes clear why it should be universal to the ocean.

Figure 6(top) shows the theoretically predicted modal branches superimposed upon Figure 3a. It clearly shows the prediction's accuracy and the association of the linear branches of Figure 3 with IW modes. It is important to note again that in the LLC4320 simulation, there is no power in the "near-inertial wedge" where high-order internal modes are found. The explanation of this observation will be seen to be especially important in all that follows. In the supporting information of this paper, we also show the dynamical equations required to describe the modes in which both κ and ν are strong functions of depth (Eqation SE10 in Supporting Information S1). In this set of equations, we also obtain the same modal alignment when we employ a depth-dependent background component similar to Equation 7. Therefore, while appropriate values for viscosity and diffusivity are critical in describing the variations of horizontal kinetic energies along each of these modal branches, as well as how damping between modes changes, no impact on the alignment of modal branches by viscosity and diffusivity terms is evident.

Because we have included damping in our Galerkin analysis, it is possible to evaluate the relative strength of damping for different modal branches. Figure 6(bottom) illustrates the variation of $\frac{\sigma_{re}}{\sigma_{lm}}$ which is a non-dimensional number that represents the attenuation per temporal frequency, as a function of the internal modal branches, derived based on the Galerkin analysis. What is calculated in Figure 6(bottom) is damping per wave period. This calculation (Equation 11) requires explicit dissipation in the model to do the analysis. For this purpose, we have employed precisely the background component of KPP that is characteristic of LLC4320 (i.e., the dotted lines in Figure 2). Because there is explicit dissipation in this analysis, it will be clear that the temporal eigenvalue must be complex and the sign of the real part of this eigenvalue must be such as to describe a damping of the IW modes as a function of time. Figure 6(bottom) demonstrates that this damping is vanishingly small for the low-order modes compared to higher-order modes. This means in LLC4320, even if there is significant forcing of these higher-order modes in what we will refer to as the "near-inertial wedge" in this diagram, we can not expect to see any well-defined IW modes to appear in the simulation. They are simply damped so strongly by the KPP background that has been employed in the simulation that they could not possibly appear.

While we have demonstrated in the above analysis that high-order modes are expected to be strongly damped in the presence of the LLC4320 background component of KPP, the most important question that will be addressed in Section 3 of this paper is: what will be the results if, in the high-resolution regional simulation, we were to remove the influence of this very high Prandtl number background, which is a characteristic of the version of KPP employed in the global model? As we will show, the elimination of this damping on the high-order modes allows

MOMENI ET AL. 11 of 23

21699291, 2024, 6, Downloaded from https://agupubs.onlinelibrary.wiley.com/doi/10.1029/2023JC02059, Wiley Online Library on [21/02/2025]. See the Terms and Conditions (https://onlinelibrary.wiley.com/terms-and-conditions) on Wiley Online Library for rules of use; OA articles are governed by the applicable Creative Commons Licensia

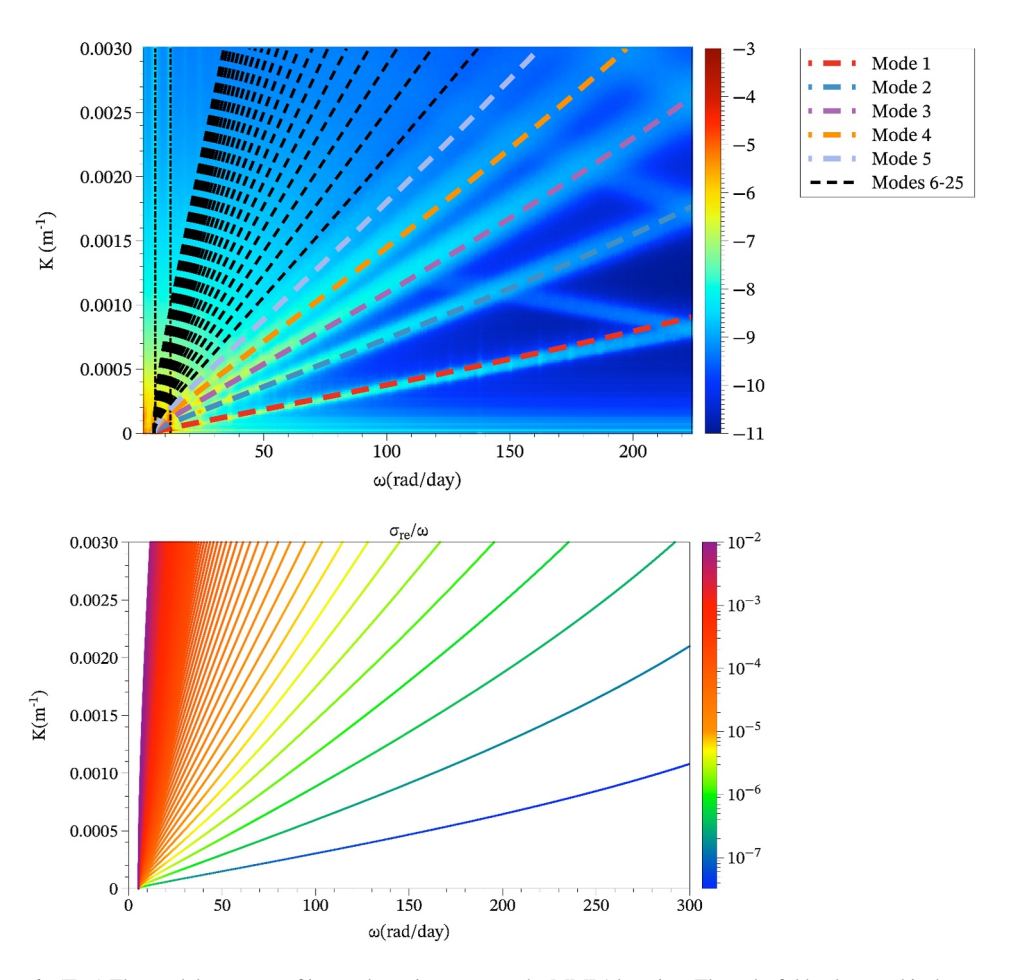


Figure 6. (Top) The modal structure of internal gravity waves at the MMP1 location. The colorful background is the same as the top-left panel of Figure 3; it shows the energy spectrum simulated with MITgcm and described in Pan et al. (2020). The dashed lines represent the modal structure obtained from Equation 11 and shown in Figure 5 (centre). (Bottom) Attenuation per period across each modal branch when depth-independent terms for viscosity and diffusivity (identical to those employed in LLC4320) are used in Equation 11. Attenuation per period is different by more than five orders of magnitude between the low-order and high-order modes.

them to participate in triad resonances with the low-order modes, which are required to support a wave-turbulence cascade.

3. Ocean Diapycnal Diffusivity: An Initial Exploration of a Modified Version of KPP

In Nelson et al. (2020), it was established that the field of hydrodynamic fluctuations in our North Pacific regional domain was clearly associated with IWs. In Section 2 above, it was demonstrated that both at the surface in terms of the spectra of Sea Surface Height squared (SSH2) and at depth in terms of the spectra of horizontal kinetic energy, the wavefield is dominated by the low-mode members of the spectrum of IWs. Here, by performing a series of both dynamically downscaled high-resolution simulations as well as a series of global-model resolution simulations of the regional domain, we will explore the extent to which an appropriately modified version of the KPP parameterization of Large et al. (1994) may be repurposed to represent the contribution to diapycnal diffusivity due to IW breaking.

3.1. Turning off the Background Component of KPP

It was previously reported in Thakur et al. (2022) that turning off the background KPP leads to more accumulation of power in the high-vertical wavenumber regime of the GM spectrum. The vertical wavenumber spectra for our series of high-resolution regional simulations are shown in Figure 7 together with the spectra for the observational MMP dataset and the GM76 predictions. Deviation of the simulation wavenumber spectrum from that of the

MOMENI ET AL. 12 of 23

21699291, 2024, 6, Downloaded from https://agupubs.onlinelibrary.wiley.com/doi/10.1029/2023JC02059, Wiley Online Library on [21/02/2025] See the Terms and Conditions (https://onlinelibrary.wiley.com/terms-and-conditions) on Wiley Online Library for rules of use; OA articles are governed by the applicable Creative Commons Licensia

Vertical wavenumber m (cpm)

Journal of Geophysical Research: Oceans

Figure 7. The solid black curve represents the slope of -2 predicted by the GM76 model. The solid red curve shows the spectra of the observational MMP3 dataset. The dashed blue curve represents the spectra for the original KPP configuration at the MMP3 location. The dashed green, purple, and orange curves represent the spectra at the MMP3 location for modified versions of KPP with the background component of KPP turned off and Ri_{ct} set to 0.7, 1.4, and 3.5, respectively. All dashed curves are based on our series of high-resolution simulations with a horizontal resolution of 250 m and 270 vertical levels.

theory was previously reported in Nelson et al. (2020), especially in the high wavenumber portion of the spectrum. Figure 7 confirms, with higher horizontal resolution than that in Thakur et al. (2022), that by turning off the background component of KPP the vertical wavenumber spectra for the highresolution regional simulations are significantly improved. Although we have confirmed the results from Thakur et al. (2022) that turning off the KPP background leads to a dramatic increase in power at high vertical wavenumber, the reason for this increase in power has never been explained. As we will show in the following paragraphs, the impact of turning off the background component of KPP on the distribution of power on individual vertical levels in the simulation will enable us to fully explain this effect upon the vertical wavenumber spectrum.

In Figure 3 of this paper, we illustrated how energy is distributed in the $K-\omega$ space for both of the runs with KPP background on and off. Figure 8 further elucidates how energy in the $K-\omega$ space redistributes when the background component of KPP is eliminated. This figure contains one of the most important findings of this paper. In Figure 8(top), we explicitly show the difference between panels (a) and (b) of Figure 3. This clearly demonstrates

that despite the observation that the differences appear small in Figure 3, these differences are nevertheless extremely important. In particular, although the internal modal branches of the low-order modes are still evident in Figures 3b and 8(top) shows that there is a significant shift of energy, in the $K-\omega$ space, into the near-inertial wedge which is entirely unpopulated by energy in the case in which the KPP background is on. A likely explanation of this shift in power from the low-order modes into the near-inertial wedge is that once the background component of turbulent diffusion of heat and momentum are eliminated from the KPP parameterization, the only remaining physical process that is active in KPP (i.e., the shear component) does not prevent energy from moving to the smallest vertical scales, as seen in Thakur et al. (2022). This increased high-m amplitude in turn enables nonlinear advective transfer from the low-m modes to the high-m modes, thereby draining energy away from the low-m modes and representing part of a cascade-like process. This is the "evidence of a wave-turbulence cascade" that is referred to in the title of this paper (Lvov et al., 2010; Pan et al., 2020). Furthermore, because these energized high-order modes in the near-inertial wedge have high vertical wavenumber, these modes are basically "carrying the shear" which enables the cascade to produce an accurate mapping using the shear component of KPP into diapycnal diffusivity. This will be discussed in detail in Section 3.2 below. Moreover, the energy of the low-m modes is decreased by approximately 15%-30% when the background component of KPP is turned off. It was previously shown that the global LLC4320 simulation contains overly strong internal tides (Arbic et al., 2022; Yu et al., 2019) and by turning off the background component of KPP in the global model, this situation could potentially be improved.

As described in the introduction section and shown in Figure 2, the background diapycnal diffusivity in the version of KPP employed in LLC4320 is characterized by a Prandtl number of Pr $\approx 1,040$. The characteristic of such a large Prandtl number is that it keeps the IW shear low by its rapid viscous diffusion, resulting in large Richardson numbers, thereby preventing IWs from breaking. The breaking is only allowed to occur when the high-Prandtl number KPP background is turned off. Clearly, a turbulence cascade from low-m to high-m modes has been enabled by the elimination of this high-Prandtl number KPP background. It is an important question as to the pathway, whereby, in this cascade, energy moves from the low-order IW modes into the near-inertial wedge of high-order modes (with high vertical wavenumbers). One suggestion that remains to be investigated in detail, concerns the possibility that this pathway may be associated with triad resonances among IWs between the loworder modes and the modes in the near-inertial wedge, which become undamped when the KPP background is turned off. One should note that "wave breaking" here is a two-step process. The first step is the mechanism whereby energy in well-resolved, low-order internal wave modes, which is stable when the high turbulent Prandtl number is active, is depleted when the KPP background is turned off. This low-mode decay does not lead to the loss of coherence of such modes from which energy is being extracted because it is occurring through resonant triad interactions. The second step involves the shear instability of the near-inertial modes energized by the first step in the process. Of course, these two steps are occurring essentially simultaneously. This mechanism of internal wave breaking is to be contrasted with the mechanism of breaking in which the wave amplitude is so large

MOMENI ET AL. 13 of 23

21699291, 2024, 6, Downloaded from https://agupubs.onlinelibrary.wiley.com/doi/10.1029/2023JC02059, Wiley Online Library on [21/02/2025] See the Terms and Conditions (https://onlinelibrary.wiley.com/terms-and-conditions) on Wiley Online Library for rules of use; OA articles are governed by the applicable Creative Commons Licensia

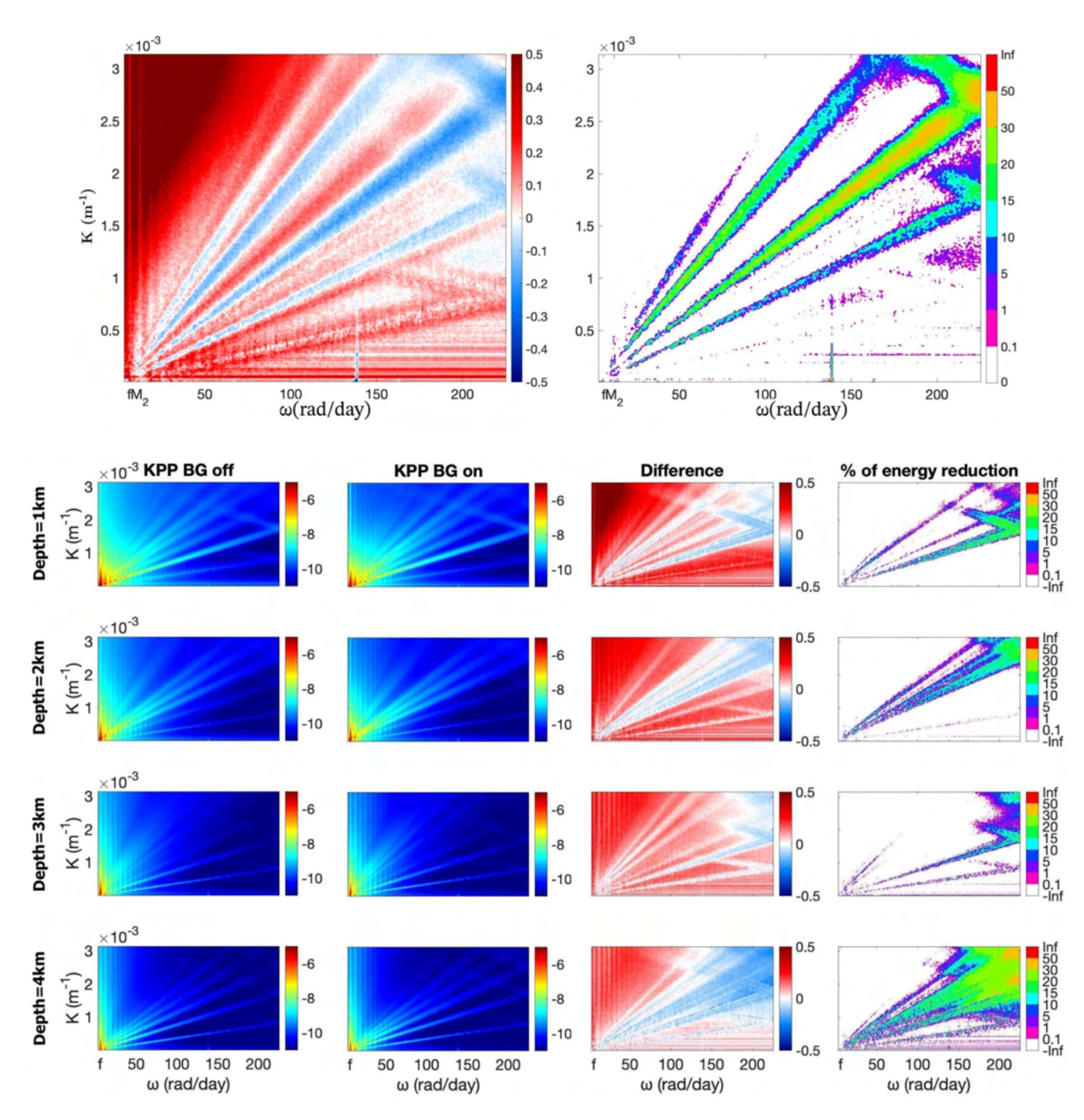


Figure 8. (Top) The energy difference in the $K-\omega$ space over a single vertical level ($z=500\,\mathrm{m}$) between the cases in which the background component of KPP is turned off and on. The left panel shows the logarithmic energy spectrum for the run with the KPP background on, and $Ri_{cr}=0.7$ subtracted from that of the run with the KPP background off, and $Ri_{cr}=0.7$; alternatively represented as $\log_{10}\left(\frac{E_{R(y=0.7)}^{B(z=0)f}(K,\omega)}{E_{R(y=0.7)}^{B(z=0)f}(K,\omega)}\right)$. The right panel demonstrates the same in the linear space (i.e., $100\times\frac{E_{R(y=0.7)}^{B(z=0)f}(K,\omega)}{E_{R(y=0.7)}^{B(z=0)f}(K,\omega)}-100$). The color bar in the right panel indicates the percentage of energy reduction in IW modal branches by turning off the background KPP. (Bottom) The first two columns represent the logarithmic energy spectrum for the cases in which the background component of KPP is turned off and on, respectively. The third column represents the difference between those logarithmic energy spaces. The fourth column represents the linear percentage reduction of energy. Each row represents a different depth level.

as to lead to an overturn of the isopycnals locally and to the development of a "patch" of intense turbulence. A detailed analysis of this mechanism in the atmospheric context of density stratified flow over localized topography is provided in Peltier and Clark (1979). The "wave-turbulence" implicated in the analyses herein is not of this conventional variety. The resonant increase of kinetic energy in the short vertical wavelength higher-order modes in the near-inertial wedge increases the vertical shear of horizontal velocity in the wavefield, leading to its increased destabilization and strongly enhanced turbulent diapycnal diffusivity. Such nonlinear triadic interactions should involve a low-m mode interacting with two high-m modes and the strength of such energy

MOMENI ET AL. 14 of 23

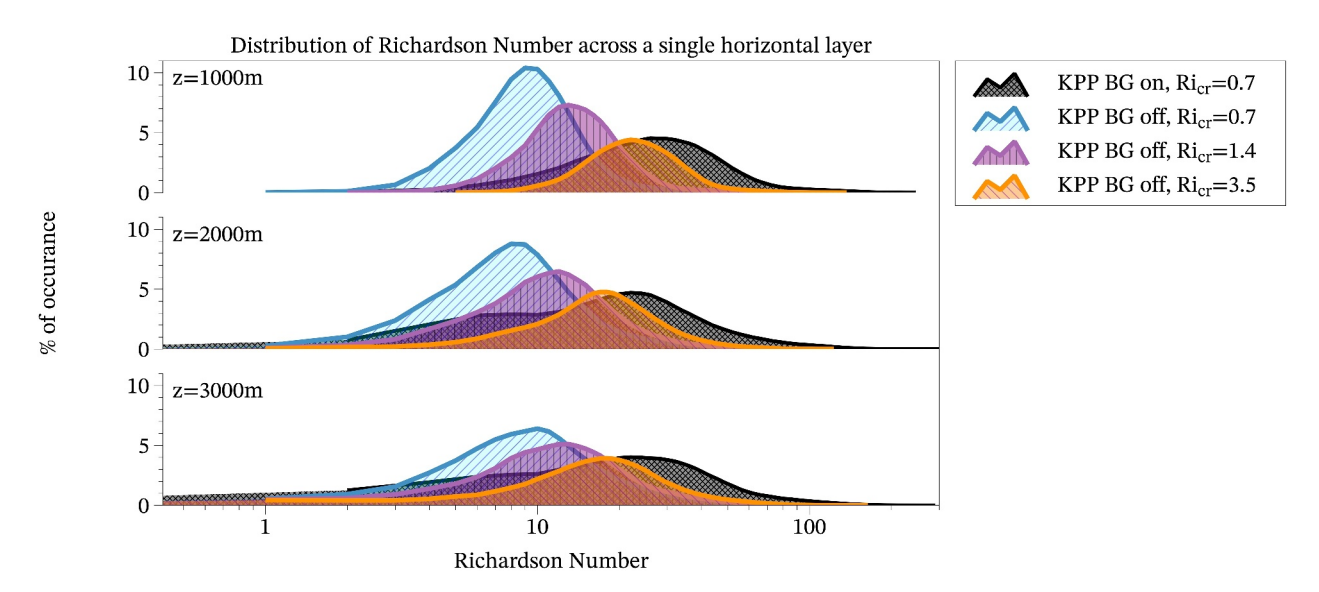


Figure 9. Distribution of time-averaged Richardson number Ri over three different single vertical levels. Evident from the plot is the log-normal behavior of the Richardson number throughout the simulation domain. Due to the fat tail of the log-normal distribution and considering that hitting a critical value is set to be the condition for the onset of turbulence in KPP, events with extremely low Richardson numbers are rare, and events with higher Richardson numbers are more frequent, thus explaining the intermittency of the turbulent events.

transfers should then scale bilinearly with two high-m amplitudes. An initial investigation of the importance of triad resonances among the IWs in this regional ocean model has been provided in Pan et al. (2020). Overall, the use of a shear-based vertical viscosity closure to dissipate energy works more effectively than a linear background vertical viscosity at representing a partial wave-turbulence cascade.

Understanding the depth dependence of wave breaking and the subsequent wave-turbulence cascade is crucial. This process involves the redistribution of horizontal kinetic energy between the low-order IW modes and the IWs within the near-inertial wedge. The significance lies in how the shear component of the KPP parameterization maps IW breaking into a depth-dependent diapycnal diffusivity. This mapping constitutes the ultimate goal of this paper, and will be the focus of Section 3.2. In Figure 8(bottom), we demonstrate that this interaction of a turbulence cascade that is mediated by the breaking of IW normal modes is not specific to the depth of z = 500 m upon which all of our previous analyses have been focused. Rather, the same interaction persists at all depths and even at the surface in terms of SSH2 spectra (as discussed in supporting information of this paper, Figure SF1 in Supporting Information S1.) This is a critical aspect of what is to follow further in Section 3.2 below. Our goal in this section is to produce a map associated with the low-order IW modes into a depth-dependent profile of diapycnal diffusivity. We will compare this depth-dependence of diapycnal diffusivity to that required by the Munk (1966) analysis. The Munk analysis is characterized by a diapycnal diffusivity in the deep ocean of approximately 1 cm²/s.

3.2. Modified KPP-Based Mapping From Internal Wave Shear to Diapycnal Diffusivity: A Tentative Exploration

The original version of the shear component of KPP was based upon the stratified parallel flow model, to which the stability theorem of Miles (1961) and Howard (1961) applies. In this model, the shear flow is demonstrated to be potentially unstable if and only if the gradient Richardson number is less than 0.25 at some height in the stratified flow. In a field of IWs, the local direction of the strongest shear is unlikely to be aligned with the local direction of the strongest stratification. In this circumstance, as we will discuss, the critical value of the Richardson number may be significantly larger than that suggested by the Miles-Howard Theorem for parallel flows.

In the shear-induced component of standard KPP, the diffusivities for both momentum and all scalars are parameterized as dependent on the local gradient Richardson number, following:

MOMENI ET AL. 15 of 23

21699291, 2024, 6, Downloaded from https://agupubs.onlinelibrary.wiley.com/doi/10.1029/2023JC020509, Wiley Online Library on [21/02/2025]. See the Terms and Conditions (https://onlinelibrary.wiley.com/doi/10.1029/2023JC020509, Wiley Online Library on [21/02/2025]. See the Terms and Conditions (https://onlinelibrary.wiley.com/doi/10.1029/2023JC020509, Wiley Online Library on [21/02/2025]. See the Terms and Conditions (https://onlinelibrary.wiley.com/doi/10.1029/2023JC020509, Wiley Online Library on [21/02/2025]. See the Terms and Conditions (https://onlinelibrary.wiley.com/doi/10.1029/2023JC020509, Wiley Online Library.wiley.com/doi/10.1029/2023JC020509, Wiley Online Lib

and-conditions) on Wiley Online Library for rules of use; OA articles are governed by the applicable Creative Commons Licenso

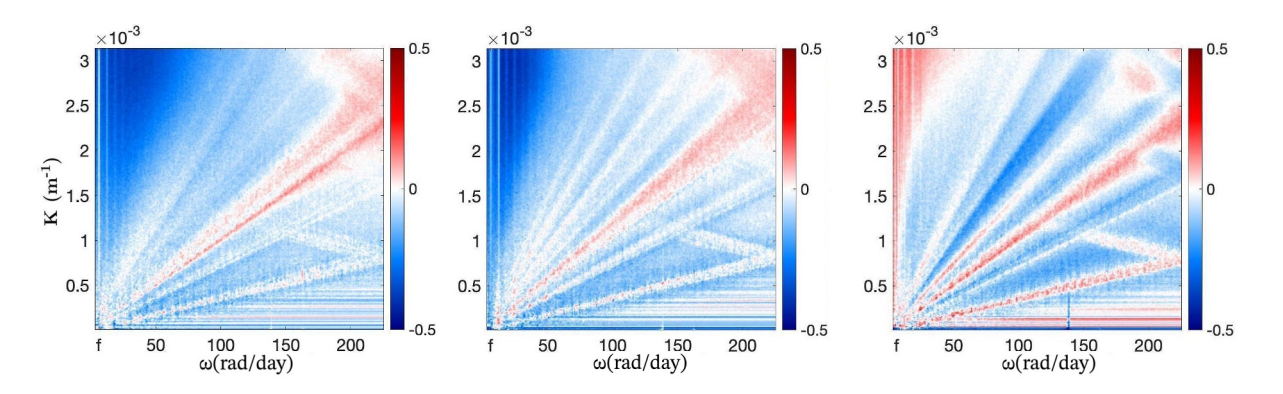


Figure 10. The logarithmic energy difference in the $K-\omega$ space at a single vertical level of z=500 m. (Left) $\log_{10}\left(\frac{E_{R(r)=1,1}^{BG-\omega f}(K,\omega)}{E_{R(r)}^{BG-\omega f}(K,\omega)}\right)$. Note that a positive red value indicates that specific modes have more energy despite the shear mechanism's increased dissipation. (Centre) illustrates $\log_{10}\left(\frac{E_{R(r)=3,5}^{BG-\omega f}(K,\omega)}{E_{R(r)=1,4}^{BG-\omega f}(K,\omega)}\right)$. And finally (Right) illustrates $\log_{10}\left(\frac{E_{R(r)=3,5}^{BG-\omega f}(K,\omega)}{E_{R(r)=1,4}^{BG-\omega f}(K,\omega)}\right)$.

$$\nu_{S} = \kappa_{S} = \nu_{0} \left(1 - \left(\frac{Ri}{Ri_{cr}} \right)^{2} \right)^{3}, \qquad 0 \le Ri < Ri_{cr}$$

$$\nu_{S} = \kappa_{S} = 0, \qquad Ri \ge Ri_{cr}$$
(14)

where the maximum value of parameterized diffusivity ν_0 and the critical Richardson number Ri_{cr} are chosen to be $\nu_0 = 50$ cm²/s and $Ri_{cr} = 0.7$ in Large et al. (1994). This parameterization form ensures rapid diffusivity growth as the Richardson number decreases below the critical value Ri_{cr} and the saturation of diffusivities at the value of ν_0 when Ri is close to 0. Although the critical Richardson number for the onset of shear instability in the stratified flow is 0.25 based on the Miles-Howard theorem (Howard, 1961; Miles, 1961), in KPP Ri_{cr} was selected to have a larger value of 0.7 to match the diffusivity-Richardson number relations post-processed from the microstructure measurements of Peters et al. (1988). It should be noted that the turbulent measurements of Peters et al. (1988) were performed in the equatorial ocean where the equatorial undercurrent induces a strong background vertical shear. This suggests that Equation 14 is initially designed based on the turbulence mixing associated with the background shear instead of the oscillating shear generated by propagating IWs.

The KPP parameterization, particularly its shear-induced mixing component described by Equation 14, may need to be revisited in our current high-resolution regional model. As the IW continuum is at least partly resolved, the shear computed at the grid scale in our model can be strongly influenced by the resolved IWs, which is clearly beyond the scope of description by Equation 14. Therefore, a revised form of shear-induced mixing needs to be considered to dissipate energy from the IW fields in our system, in which the value of the critical Richardson number Ri_{cr} in Equation 14 needs to be adjusted.

Insights on the value of Ri_{cr} in the IW-resolving models have been provided in at least two lines of research in the literature. The first line of research is the parcel-based argument performed by Hines (1971). In this work, the energetics of fluid-parcel exchange have been analyzed in the stratified flow. For a system in which the density gradient is strictly aligned in the vertical direction, Hines (1971)'s analysis reproduced the conclusion of the Miles-Howard theorem; namely, the flow is energetically stable if the Richardson number associated with the shear is larger than 0.25. However, in the case in which the density gradient is slightly tilted from the vertical direction (as in the case of isopycnal surfaces perturbed by the IWs) the system becomes inherently unstable from the energy perspective. The critical value of $Ri_{cr} = 0.25$ provides a criterion that is too strict for the instability to occur. This fact can also be demonstrated by the linear stability analyses performed on the monochromatic IW (e.g., Lombard and Riley (1996); Sonmor and Klaassen (1997)). These studies established a complicated picture of different types of fluid-dynamical instabilities that act to break the IWs, which showed that instabilities might occur even if the Richardson number is larger than 0.25.

MOMENI ET AL. 16 of 23

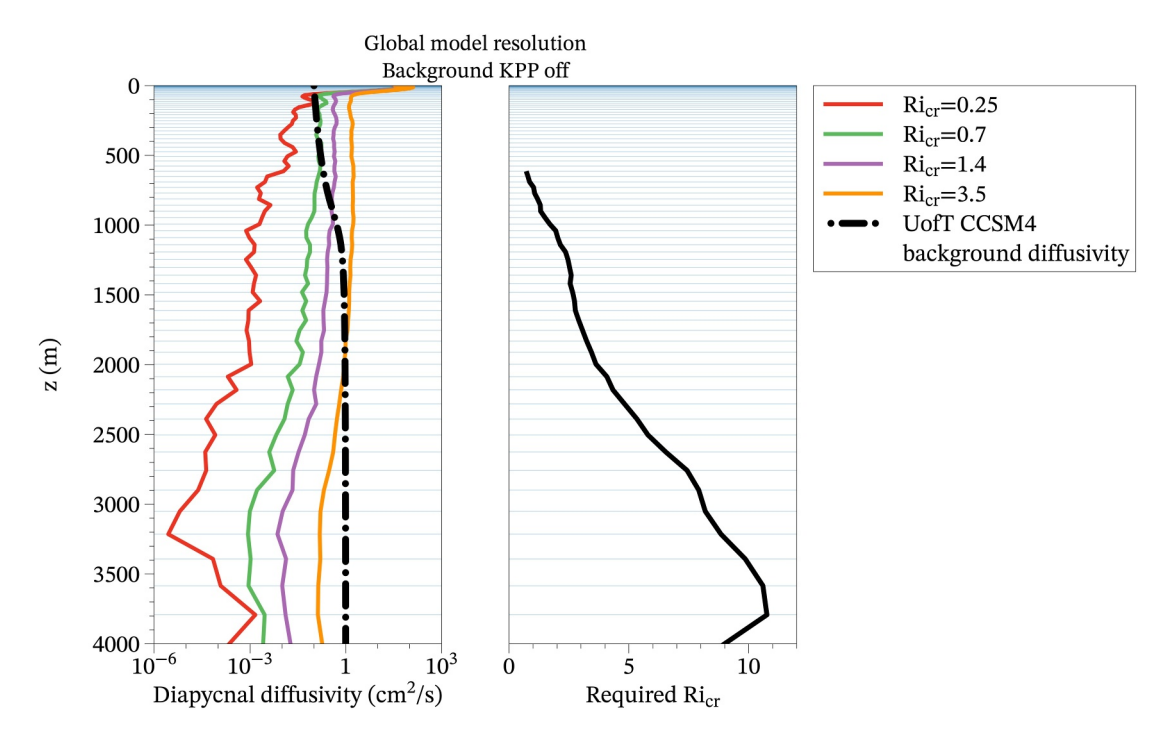


Figure 11. Left panel shows the depth dependence profiles of diapycnal diffusivity over the regional domain for a series of experiments with the global model resolution. The black dashed-dotted curve represents a standard background diffusivity, typically used in the ocean component of a low-resolution climate simulation. The thin horizontal blue lines represent the midpoint of each vertical depth level in the simulations. The right panel shows the required value for the critical Richardson number Ri_{cr} to generate, on average, the target value used in the parameterized background component of Equation 7 at each depth level.

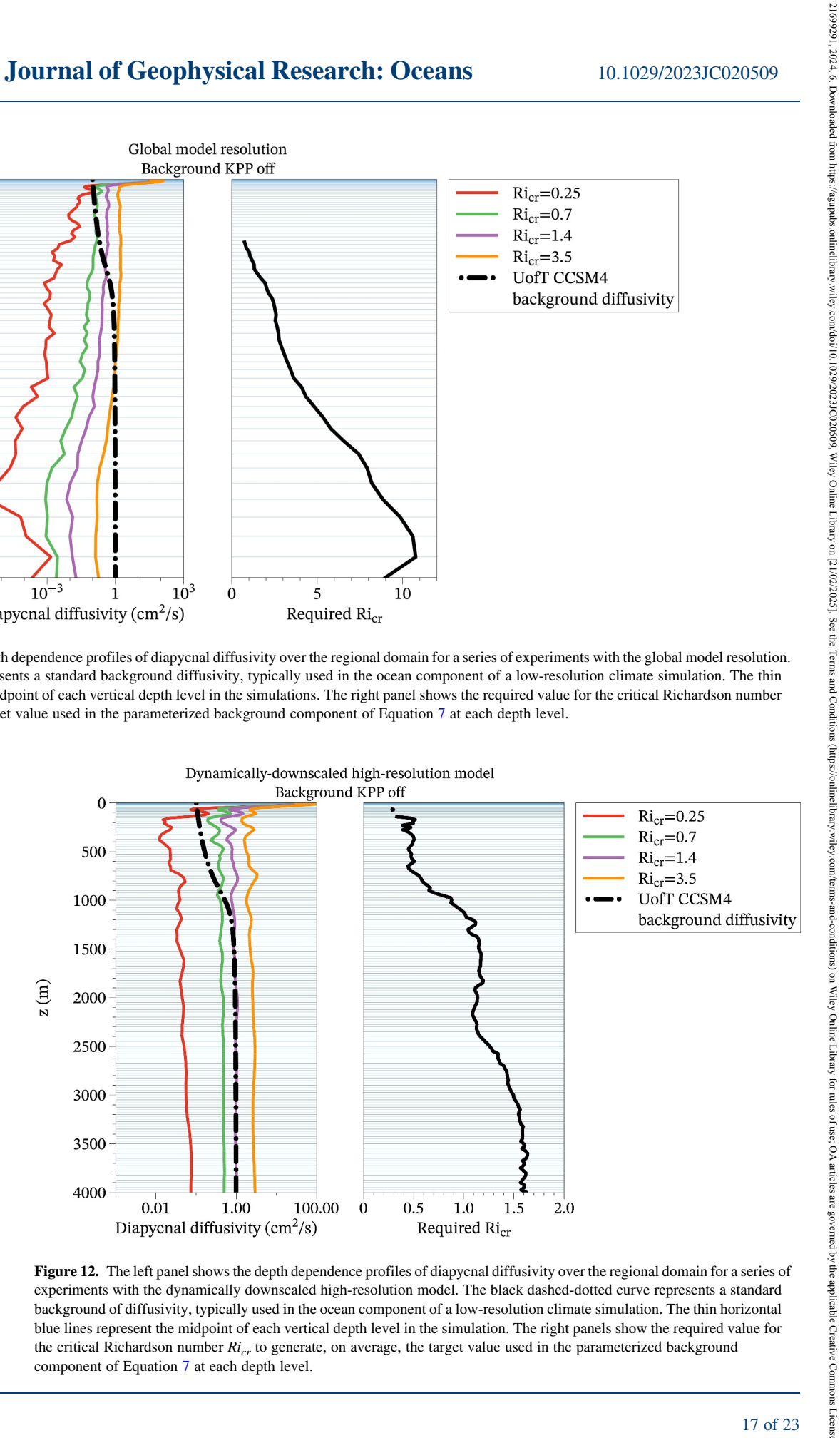


Figure 12. The left panel shows the depth dependence profiles of diapycnal diffusivity over the regional domain for a series of experiments with the dynamically downscaled high-resolution model. The black dashed-dotted curve represents a standard background of diffusivity, typically used in the ocean component of a low-resolution climate simulation. The thin horizontal blue lines represent the midpoint of each vertical depth level in the simulation. The right panels show the required value for the critical Richardson number Ri_{cr} to generate, on average, the target value used in the parameterized background component of Equation 7 at each depth level.

MOMENI ET AL. 17 of 23



Journal of Geophysical Research: Oceans

10.1029/2023JC020509

While the above studies showed that the criterion for the onset of instabilities is generally looser in the context of IW breaking, the proper value for Ri_{cr} that needs to be implemented in our high-resolution regional model remains unclear. Therefore, by changing the background component of KPP and the critical Richardson number in Equation 14 to several values larger than 0.7, we have performed several comparison experiments to study the influences of this number in our model.

Figure 9 sheds further light on the physical origins of the shear mechanism of KPP by plotting the distributions of time-averaged Richardson number Ri for this series of dynamically downscaled regional experiments. As previously mentioned, the large Prandtl number employed in LLC4320 keeps the shear low by its high viscous diffusion. Richardson number $Ri = \frac{bouyancy\ term}{flow\ shear\ term} = \frac{g}{\rho} \frac{\partial \rho / \partial z}{(\partial u / \partial z)^2}$ which controls the shear component of KPP is a ratio of two gradients: density gradient and the square of momentum gradient. Prandtl number, on the other hand, is a ratio of two diffusion coefficients: momentum diffusion and thermal diffusion. The numerator of the latter is related to the denominator of the former, and vice versa. It's important to note that we are referring to the "turbulent" Prandtl number, a discussion of which is provided in Salehipour and Peltier (2015). Therefore, the way that thermal diffusivity controls the rate of diffusion of the density gradient is, of course, exerted by the turbulent diffusivity of density; just as it is the turbulent momentum diffusivity that controls the rate of diffusion of the velocity gradient that appears in the denominator of the definition of the Richardson number. When the Prandtl number is large, momentum is diffused at a larger rate compared to density, which in turn, leads to lower shear compared to buoyancy. This mechanism ultimately keeps the Richardson number high and prevents the shear term of KPP from activity. Note that the dependency of the Richardson number on the shear is nonlinear and this nonlinearity accentuates the impact of the high-Prandtl number on the Richardson number. Figure 9 makes it clear that by turning off this high-Prandtl number background, the distribution of the Richardson number is significantly shifted to the left, allowing for higher shear activity and, subsequently, more parameterized IW breaking. However, as the critical Richardson number Ri_{cr} increases, the average Richardson number returns to the right. This is because by increasing the critical Richardson number Ri_{cr} , the condition for the onset of the shear component is loosened, and the shear component of KPP acts more frequently, resulting in a more stable ocean with higher Richardson numbers. Having a too-tight value for Ri_{cr}, fails to allow the build-up of the required global average background diffusivity and viscosity in the ocean, whereas having an overly loose condition might suppress the development of IWs and shear activity. After turning off the background component of KPP, coming up with the optimized value of the critical Richardson number Ri_{cr} seems to be a necessary next step.

Figure 10 demonstrates the effects of increasing the critical Richardson number Ri_{cr} on the quality of expression of IW modes. The left and the middle panels show that after turning off the background component of KPP, by merely increasing the critical Richardson number, first from $Ri_{cr} = 0.7$ to $Ri_{cr} = 1.4$ and then from $Ri_{cr} = 1.4$ to $Ri_{cr} = 3.5$, low-order modal branches would become more energetic. The right panel, on the other hand, shows the effect of both turning off the background component of KPP and increasing the critical Richardson number from $Ri_{cr} = 0.7$ to $Ri_{cr} = 3.5$ simultaneously: a clearer presence of low-mode IWs is observed without the suppression of energy in the near-inertial wedge. However, Figure 7 made it clear that increasing the critical Richardson number as a fixed parameter for the whole ocean does not improve the wavenumber spectra. Hence, a closer look at the impact of the critical Richardson number on the profiles of diapycnal diffusivity is needed.

The depth dependence of diapycnal diffusivity profiles for our series of experiments is shown in the left panels of Figures 11 and 12. All the profiles are averaged over the regional domain and 20 simulation days. Figure 11 shows the results for the simulations in which the resolution is set to be the same as in the global LLC4320 model, albeit run over the regional domain. In contrast, Figure 12 shows the results for the regional model in its highest resolution. In both figures, the midpoints of vertical depth levels are shown in thin horizontal blue lines to demonstrate the vertical resolution. It is clear from Figure 12 that when the background component is turned off, contrary to initial expectations, the diffusivity profile is not inhibited but is actually enhanced and shifted to the right. This is clear supporting evidence for the finding of Figure 8; in the high-resolution simulation, when the background component of KPP is turned off, the model allows the development of parameterized breaking IWs, which in turn produces more shear and ultimately leads to higher diffusivity. Turning off the background component of KPP also ensures that the resulting diffusivity and viscosity are mainly shear-induced because the convective component of KPP acts much less frequently than its shear counterpart. Now, by changing the critical Richardson number Ri_{cr} in the model and comparing it with the University of Toronto version of the NCAR CCSM4 depth-dependent background component of KPP (see Equation 7), we explore whether or not the shear-

MOMENI ET AL. 18 of 23

onlinelibrary wiley.com/doi/10.1029/2023JC020509, Wiley Online Library on [21/02/2025]. See the Terms and Conditions (https://onlinelibrary.wiley.com/

induced mixing might be able to describe the background diapycnal diffusivity in the ocean. The right panels of Figures 11 and 12 show that it would be possible to build up the target background diffusivity by increasing Ri_{cr} . However, in its conventional form, KPP might be unable to provide an accurate map from the Richardson number to the diapycnal diffusivity.

It is generally understood that the intensity of turbulent mixing would increase as the value of the critical Richardson number Ri_{cr} increased. However, the critical Richardson number Ri_{cr} on the basis of which the intensity of turbulent mixing may be parameterized is not fixed. Hence, in the analysis to follow, we suggest a tentative approach in which the arbitrariness of Ri_{cr} is exploited, and the possibility of its depth dependence is allowed. To get a more accurate estimation of what range of values for Ri_{cr} is needed to achieve the target background level of diffusivity of Equation 7, a further number of simulations with different values of Ri_{cr} are performed. Then, for each depth level, a linear interpolation is used to determine the optimum fit value of Ri_{cr} that results in the target diffusivity level described in Equation 7. The right panel of Figure 11 summarizes the result of this optimal fit for the simulations in which the resolution is set to be the same as in the global model, albeit run over the regional domain. It is clear from the figure that, in the low-resolution simulation, the variation in the critical Richardson number Ri_{cr} that is needed to build up the target diffusivity is very large and is extended to unreasonably high values of Ri_{cr} in the deep ocean. Therefore, the KPP's shear component in the low-resolution global simulation cannot accurately map the parameterized IW-breaking process into a depth dependence of diapycnal diffusivity.

However, the same experiment with the high-resolution simulation indicates a much more confined range of required critical Richardson number Ri_{cr} . The result for the high-resolution model is shown in the right panel of Figure 12. As the plot suggests, in the high-resolution simulations where the wave-breaking process is adequately resolved, a modest change in Ri_{cr} can hit the target of Equation 7 and explain the observed average background diffusivity in the ocean. It is unclear whether the required critical Richardson number Ri_{cr} converges to a fixed depth-independent value as the resolution is further increased or if it would instead form a mild increasing trend with depth. Neither is it clear how this trend holds in different geographical locations, and such questions should be investigated further through this suggested approach.

4. Conclusion

Our goal in the present paper has been to explore the extent to which recent advances in ocean general circulation modeling might enable the development of a mechanistic connection between the parameterized "breaking" of ocean IWs and diapycnal diffusivity. Our analyses have relied upon the availability of high-resolution global integrations that have been explicitly forced by the astronomical tidal potential as well as by the atmosphere. The incorporation of simultaneous tidal and atmospheric forcing is especially critical as the most important sources of ocean IWs involve the interaction of the barotropic M2 tide with bottom topography as well as the generation of near-inertial waves by the high-frequency component of the wind field. The interactions between near-inertial waves, internal tides, and, possibly, mesoscale eddies, excite a family of internal waves. For the purpose of this paper, a particular high-resolution global model integration has been critical to our analyses, namely that referred to in the literature as MITgcm48 or LLC4320, a model with approximately 2 km horizontal resolution at the equator. Equally important as this high horizontal resolution, however, is that this model integration was conducted with a special version of the KPP parameterization of diapycnal diffusivity in which the background component was set to a depth-independent form in which the diffusivities for both momentum and heat were set to values that are much lower than previously expected, but characterized by a ratio, the Prandtl number that was very large. The background diapycnal diffusivity was so low that the model could not have operated in climate mode because, in that mode, a diapycnal diffusivity of approximately 1 cm²/s is required to support the Meridional Overturning Circulation (MOC). Because of the manner in which it has been configured, this model offers a unique opportunity for detailed analyses of IW-related processes.

The first indication of the model's usefulness for such purposes was provided in the paper of Pan et al. (2020). In their Figure 8, it was shown that when the results of the global model were dynamically downscaled into a regional domain, 6° by 8° in horizontal extent, in which the horizontal resolution was increased by a further factor of 8-250 m, the IW field was shown to be especially well resolved with the first five of the lowest order internal wave modes resolved and their energy levels at a depth of 500 m determined as a function of horizontal wavenumber and temporal frequency. The analyses in Section 2 of this paper have shown that the modal lines on which

MOMENI ET AL. 19 of 23

horizontal kinetic energy is concentrated are accurately predicted by a Galerkin analysis of the Sturm-Liouville problem when the length scale on which the modal structure is quantized is equal to the bathymetric depth characteristic of the high-resolution regional domain. It was also shown that the basic modal structure was unaffected by the background component of the KPP parameterization employed in LLC4320.

However, this was not the case when one focuses on the energy levels along the individual modal branches in the $K-\omega$ space. When the background component of KPP was left on in the high-resolution regional domain, the distribution of the spectra of horizontal kinetic energy was almost entirely confined to the modal lines characteristic of the first five or so lowest-order modes. All of the energy in the wedge-shaped region in which the higher-order modes were expected to exist was shown to be "trapped" near the origin in $K - \omega$ space. However, when the background component of KPP employed in LLC4320 was turned off in the high-resolution domain, the energy levels of the lower-order modes dropped, and a dramatic increase in energy occurred in the wedge-shaped region in which the higher-order modes were predicted to exist, where the IWs are near-inertial. The high-order modes were clearly being damped by the action of the background component of KPP. When this influence is eliminated, parameterized breaking occurs through the action of the only remaining component of KPP, namely the shear component. Because the higher-order modes are characterized by increased vertical shear in horizontal velocity, the transfer of energy to these modes results in a sharp decrease in the Richardson number in the field of internal waves. Therefore, when these high-wavenumber modes in the near-inertial wedge become undamped through the elimination of the background component of KPP, energy cascades are able to produce a more accurate mapping from the shear component of KPP into diapycnal diffusivity. The shear component of KPP would be expected to capture the parameterized IW-breaking process. Therefore, we explored what this mapping would predict for ocean diapycnal diffusivity produced by breaking IWs.

The pathway whereby the higher order modes in the near-inertial wedge become energized is one of the most important results of our analyses together with those for the depth dependence of diapycnal diffusivity to be expected due to internal wave breaking. Our results strongly suggest that this pathway involves triad interactions between a low-order internal mode having a low vertical wavenumber m and two high vertical wavenumber modes from the near-inertial wedge, the latter being energized by the loss of energy from the former. In work to be discussed elsewhere, we will provide detailed analyses of these triad interactions. The fact that the higher order modes are able to participate in triad resonant interactions when the KPP background is eliminated has been fully explained herein. The high Prandtl number background of the global model plays a crucial role in this explanation. It endows the higher order modes with strong temporal damping, thereby making resonant interactions with them impossible.

In exploring the mapping from the shear component of KPP to diapycnal diffusivity, we first had to recognize the arbitrariness of the assumptions on the basis of which the shear component of KPP was constructed. In particular, the assumption that a shear flow would be dynamically unstable if the gradient Richardson number was less than the critical value of $Ri_{cr} = 0.7$ was based upon a weak justification, suggesting that the exact result for parallel flows, provided by the Miles-Howard Theorem for which the critical value is 0.25, required modification. It is clearly a significant question as to whether a parallel flow analogy, even one that has been arbitrarily adjusted as in KPP, is appropriate to the development of a reliable understanding as to how this process should map into diapycnal diffusivity. We pointed to the analysis of Hines (1971) to suggest that a further raising of the critical Richardson number might make the shear component of KPP more appropriate to the case of parameterized IW breaking. The Hines analysis, which was based upon the application of a parcel method, suggested that if surfaces of constant shear and constant stratification were misaligned, as they are not in a parallel flow model, then depending upon the degree of misalignment, the critical value of the Richardson number could be arbitrarily large. This further modification of KPP may provide a more accurate way of mapping IW shear into breaking waveinduced diapycnal diffusivity.

The final, and perhaps the most important result of this paper, concerned the mechanistic prediction of the depth dependence of diapycnal diffusivity expected to exist due to the breaking of internal waves, as parameterized on the basis of an appropriately adjusted representation of the KPP mapping from this component of KPP into diapycnal diffusivity. We demonstrated that, with only a minor further adjustment to the critical Richardson number assumed in this mapping, when it was applied to the high-resolution downscaled simulation in the regional domain, it delivered a prediction of abyssal ocean diapycnal diffusivity that fits the Munk (1966) constraint required to explain how the deep water that forms at the poles is able to upwell back to the surface, thus

MOMENI ET AL. 20 of 23

21699291, 2024, 6, Downloaded from https://agupubs.onlinelibrary.wiley.com/doi/10.1029/2023IC020509, Wiley Online Library on [21/02/2025]. See the Terms and Conditions (https://onlinelibrary.wiley.com/terms

and-conditions) on Wiley Online Library for rules of use; OA articles are governed by the applicable Creative Commons License

closing the meridional overturning circulation (MOC) of the oceans. Although it is generally believed that this must be the case, our analysis appears to be the first to demonstrate this mechanistically.

Acronyms

IW Internal wave

GM The Garrett-Munk spectrum

KPP The Kappa-profile parameterization

CESM The Community Earth System Model

NCAR The US National Center for Atmospheric Research

MITgcm Massachusetts Institute of Technology general circulation model

HYCOM HYbrid Coordinate Ocean Model

MMP McLane Moored Profiler

ECMWF European Center for Medium-Range Weather Forecasts

LLC4320 Same as MITgcm48, the global ocean model forced by both winds and tides

CCSM4 The Community Climate System Model

MOC Meridional Overturning Circulation

Data Availability Statement

The diapycnal diffusivity data for different values of critical Richardson number on the basis of which the analysis presented in this paper have been performed are available at Momeni et al. (2024) (https://doi.org/10.7910/DVN/RZUCLE).

Acknowledgments References

All the simulations in this study were

maintained by the SciNet facility, a

component of the Digital Research

Alliance of Canada located at the

performed on the Niagara supercomputer,

University of Toronto. The graphics were

generated using DataGraph, Version 5.0.

RT, BKA, and JS acknowledge support

Research Grant N00014-19-1-2712. WRP was supported by the Natural Sciences and

Engineering Research Council of Canada

under the NSERC Discovery Grant A9627.

DM carried out research at JPL. Caltech.

under contract with NASA, with support

from the Physical Oceanography and

Programs. The MP observations from

Alford et al. (2007) were funded by NSF.

Modeling, Analysis, and Prediction

from NASA Grant 80NSSC20K1135, National Science Foundation (NSF) grant

OCE-1851164, and Office of Naval

Alford, M. H., MacKinnon, J. A., Zhao, Z., Pinkel, R., Klymak, J., & Peacock, T. (2007). Internal waves across the pacific. *Geophysical Research Letters*, 34(24). https://doi.org/10.1029/2007gl031566

Alford, M. H., & Pinkel, R. (2000). Observations of overturning in the thermocline: The context of ocean mixing. *Journal of Physical Ocean-ography*, 30(5), 805–832. https://doi.org/10.1175/1520-0485(2000)030<0805:oooitt>2.0.co;2

Andrews, T., Gregory, J. M., Paynter, D., Silvers, L. G., Zhou, C., Mauritsen, T., et al. (2018). Accounting for changing temperature patterns increases historical estimates of climate sensitivity. *Geophysical Research Letters*, 45(16), 8490–8499. https://doi.org/10.1029/2018gl078887Arbic, B. K., Alford, M. H., Ansong, J. K., Buijsman, M. C., Ciotti, R. B., Farrar, J. T., et al. (2018). A primer on global internal tide and internal gravity wave continuum modeling in hycom and mitgcm. *New Frontiers in Operational Oceanography*. https://doi.org/10.17125/gov2018.

Arbic, B. K., Elipot, S., Brasch, J. M., Menemenlis, D., Ponte, A. L., Shriver, J. F., et al. (2022). Near-surface oceanic kinetic energy distributions from drifter observations and numerical models. *Journal of Geophysical Research: Oceans*, 127(10), e2022JC018551. https://doi.org/10.1029/2022jc018551

Baker, M. A., & Gibson, C. H. (1987). Sampling turbulence in the stratified ocean: Statistical consequences of strong intermittency. *Journal of Physical Oceanography*, 17(10), 1817–1836. https://doi.org/10.1175/1520-0485(1987)017<1817:stitso>2.0.co;2

Bleck, R. (2002). An oceanic general circulation model framed in hybrid isopycnic-cartesian coordinates. *Ocean Modelling*, 4(1), 55–88. https://doi.org/10.1016/s1463-5003(01)00012-9

Bryan, K., & Lewis, L. (1979). A water mass model of the world ocean. *Journal of Geophysical Research*, 84(C5), 2503–2517. https://doi.org/10.1029/jc084ic05p02503

Cairns, J. L., & Williams, G. O. (1976). Internal wave observations from a midwater float, 2. Journal of Geophysical Research, 81(12), 1943–1950. https://doi.org/10.1029/jc081i012p01943

Dong, Y., Proistosescu, C., Armour, K. C., & Battisti, D. S. (2019). Attributing historical and future evolution of radiative feedbacks to regional warming patterns using a green's function approach: The preeminence of the western pacific. *Journal of Climate*, 32(17), 5471–5491. https://doi.org/10.1175/jcli-d-18-0843.1

Garrett, C. (2003). Internal tides and ocean mixing. Science, 301(5641), 1858–1859. https://doi.org/10.1126/science.1090002

Garrett, C., & Munk, W. (1971). Internal wave spectra in the presence of fine-structure. *Journal of Physical Oceanography*, 1(3), 196–202. https://doi.org/10.1175/1520-0485(1971)001<0196:iwsitp>2.0.co;2

Garrett, C., & Munk, W. (1972). Space-time scales of internal waves. Geophysical Fluid Dynamics, 3(3), 225–264. https://doi.org/10.1080/03091927208236082

Garrett, C., & Munk, W. (1975). Space-time scales of internal waves: A progress report. *Journal of Geophysical Research*, 80(3), 291–297. https://doi.org/10.1029/jc080i003p00291

MOMENI ET AL. 21 of 23

- Gaspar, P., Grégoris, Y., & Lefevre, J.-M. (1990). A simple eddy kinetic energy model for simulations of the oceanic vertical mixing: Tests at station papa and long-term upper ocean study site. *Journal of Geophysical Research*, 95(C9), 16179–16193. https://doi.org/10.1029/jc095ic09p16179
- Gula, J., & Peltier, W. (2012). Dynamical downscaling over the great lakes basin of north America using the wrf regional climate model: The impact of the great lakes system on regional greenhouse warming. *Journal of Climate*, 25(21), 7723–7742. https://doi.org/10.1175/jcli-d-11-00388
- Hines, C. (1971). Generalizations of the richardson criterion for the onset of atmospheric turbulence. Quarterly Journal of the Royal Meteorological Society, 97(414), 429–439. https://doi.org/10.1002/qj.49709741405
- Howard, L. N. (1961). Note on a paper of john w. miles. Journal of Fluid Mechanics, 10(4), 509-512. https://doi.org/10.1017/s0022112061000317
- Kundu, P. K., Cohen, I. M., & Dowling, D. R. (2015). Fluid mechanics. Academic press.
- Lamb, K. G. (2014). Internal wave breaking and dissipation mechanisms on the continental slope/shelf. Annual Review of Fluid Mechanics, 46(1), 231–254. https://doi.org/10.1146/annurev-fluid-011212-140701
- Large, W. G., McWilliams, J. C., & Doney, S. C. (1994). Oceanic vertical mixing: A review and a model with a nonlocal boundary layer parameterization. Reviews of Geophysics, 32(4), 363–403. https://doi.org/10.1029/94rg01872
- Lombard, P. N., & Riley, J. J. (1996). Instability and breakdown of internal gravity waves. i. linear stability analysis. *Physics of Fluids*, 8(12), 3271–3287. https://doi.org/10.1063/1.869117
- Losch, M., Menemenlis, D., Campin, J.-M., Heimbach, P., & Hill, C. (2010). On the formulation of sea-ice models. part 1: Effects of different solver implementations and parameterizations. *Ocean Modelling*, 33(1–2), 129–144. https://doi.org/10.1016/j.ocemod.2009.12.008
- Lvov, Y. V., Polzin, K. L., Tabak, E. G., & Yokoyama, N. (2010). Oceanic internal-wave field: Theory of scale-invariant spectra. *Journal of Physical Oceanography*, 40(12), 2605–2623. https://doi.org/10.1175/2010jpo4132.1
- MacKinnon, J. A., Zhao, Z., Whalen, C. B., Waterhouse, A. F., Trossman, D. S., Sun, O. M., et al. (2017). Climate process team on internal wave-driven ocean mixing. Bulletin of the American Meteorological Society, 98(11), 2429–2454. https://doi.org/10.1175/bams-d-16-0030.1
- Marshall, J., Adcroft, A., Hill, C., Perelman, L., & Heisey, C. (1997). A finite-volume, incompressible Navier Stokes model for studies of the ocean on parallel computers. *Journal of Geophysical Research*, 102(C3), 5753–5766. https://doi.org/10.1029/96jc02775
- Mellor, G. L., & Yamada, T. (1982). Development of a turbulence closure model for geophysical fluid problems. *Reviews of Geophysics*, 20(4),
- 851–875. https://doi.org/10.1029/rg020i004p00851 Miles, J. W. (1961). On the stability of heterogeneous shear flows. *Journal of Fluid Mechanics*, 10(4), 496–508. https://doi.org/10.1017/
- s0022112061000305

 Momeni, K., Ma, Y., Peltier, W., Menemenlis, D., Thakur, R., Pan, Y., et al. (2024). Data repository for breaking internal waves and Ocean Diapycnal diffusivity in a high-resolution Regional Ocean Model: Evidence of a wave-turbulence cascade [dataset]. https://doi.org/10.7910/DVN/RZUCLE. Harvard Dataverse.
- Müller, M., Arbic, B. K., Richman, J. G., Shriver, J. F., Kunze, E. L., Scott, R. B., et al. (2015). Toward an internal gravity wave spectrum in global ocean models. *Geophysical Research Letters*, 42(9), 3474–3481. https://doi.org/10.1002/2015gl063365
- Munk, W. H. (1966). Abyssal recipes. Deep-Sea Research and Oceanographic Abstracts, 13(4), 707–730. https://doi.org/10.1016/0011-7471(66)
- Nelson, A., Arbic, B. K., Menemenlis, D., Peltier, W., Alford, M. H., Grisouard, N., & Klymak, J. (2020). Improved internal wave spectral continuum in a regional ocean model. *Journal of Geophysical Research: Oceans*, 125(5), e2019JC015974. https://doi.org/10.1029/2019jc015974
- Nguyen, A. T., Menemenlis, D., & Kwok, R. (2009). Improved modeling of the Arctic halocline with a subgrid-scale brine rejection parameterization. *Journal of Geophysical Research*, 114(C11), C11014. https://doi.org/10.1029/2008jc005121
- Nguyen, A. T., Menemenlis, D., & Kwok, R. (2011). Arctic ice-ocean simulation with optimized model parameters: Approach and assessment. Journal of Geophysical Research, 116(C4), C04025. https://doi.org/10.1029/2010jc006573
- Pacanowski, R., & Philander, S. (1981). Parameterization of vertical mixing in numerical models of tropical oceans. *Journal of Physical Oceanography*, 11(11), 1443–1451. https://doi.org/10.1175/1520-0485(1981)011<1443:povmin>2.0.co;2
- Pan, Y., Arbic, B. K., Nelson, A. D., Menemenlis, D., Peltier, W., Xu, W., & Li, Y. (2020). Numerical investigation of mechanisms underlying oceanic internal gravity wave power-law spectra. *Journal of Physical Oceanography*, 50(9), 2713–2733. https://doi.org/10.1175/jpo-d-20-0030-1
- Pan, Y., Haley, P. J., & Lermusiaux, P. F. (2021). Interactions of internal tides with a heterogeneous and rotational ocean. *Journal of Fluid Mechanics*, 920. A18. https://doi.org/10.1017/ffm.2021.423
- Peltier, W., & Clark, T. (1979). The evolution and stability of finite-amplitude mountain waves. part ii: Surface wave drag and severe downslope windstorms. *Journal of the Atmospheric Sciences*, 36(8), 1498–1529. https://doi.org/10.1175/1520-0469(1979)036<1498:teasof>2.0.co;2
- Peltier, W., Ma, Y., & Chandan, D. (2020). The kpp trigger of rapid amoc intensification in the nonlinear dansgaard-oeschger relaxation oscillation. *Journal of Geophysical Research: Oceans*, 125(5), e2019JC015557. https://doi.org/10.1029/2019jc015557
- Peltier, W., & Vettoretti, G. (2014). Dansgaard-oeschger oscillations predicted in a comprehensive model of glacial climate: A "kicked" salt oscillator in the atlantic. Geophysical Research Letters, 41(20), 7306–7313. https://doi.org/10.1002/2014gl061413
- Peters, H., Gregg, M., & Toole, J. (1988). On the parameterization of equatorial turbulence. *Journal of Geophysical Research*, 93(C2), 1199–1218. https://doi.org/10.1029/jc093ic02p01199
- Ponte, R. M., Chaudhuri, A. H., & Vinogradov, S. V. (2015). Long-period tides in an atmospherically driven, stratified ocean. *Journal of Physical Oceanography*, 45(7), 1917–1928. https://doi.org/10.1175/jpo-d-15-0006.1
- Rocha, C. B., Chereskin, T. K., Gille, S. T., & Menemenlis, D. (2016). Mesoscale to submesoscale wavenumber spectra in drake passage. *Journal of Physical Oceanography*, 46(2), 601–620. https://doi.org/10.1175/jpo-d-15-0087.1
- Salehipour, H., & Peltier, W. (2015). Diapycnal diffusivity, turbulent Prandtl number and mixing efficiency in boussinesq stratified turbulence. Journal of Fluid Mechanics, 775, 464–500. https://doi.org/10.1017/jfm.2015.305
- Savage, A. C., Arbic, B. K., Alford, M. H., Ansong, J. K., Farrar, J. T., Menemenlis, D., et al. (2017). Spectral decomposition of internal gravity wave sea surface height in global models. *Journal of Geophysical Research: Oceans*, 122(10), 7803–7821. https://doi.org/10.1002/2017jc013009
- Schiller, A., & Fiedler, R. (2007). Explicit tidal forcing in an ocean general circulation model. Geophysical Research Letters, 34(3). https://doi.org/10.1029/2006g1028363
- Siyanbola, O. Q., Buijsman, M. C., Delpech, A., Renault, L., Barkan, R., Shriver, J. F., et al. (2023). Remote internal wave forcing of regional ocean simulations near the us west coast. *Ocean Modelling*, 181, 102154. https://doi.org/10.1016/j.ocemod.2022.102154

MOMENI ET AL. 22 of 23

- Sonmor, L., & Klaassen, G. (1997). Toward a unified theory of gravity wave stability. *Journal of the Atmospheric Sciences*, 54(22), 2655–2680. https://doi.org/10.1175/1520-0469(1997)054<2655:tautog>2.0.co;2
- Thakur, R., Arbic, B. K., Menemenlis, D., Momeni, K., Pan, Y., Peltier, W., et al. (2022). Impact of vertical mixing parameterizations on internal gravity wave spectra in regional ocean models. *Geophysical Research Letters*, 49(16), e2022GL099614. https://doi.org/10.1029/2022gl099614
- Thomas, M., Sündermann, J., & Maier-Reimer, E. (2001). Consideration of ocean tides in an ogcm and impacts on subseasonal to decadal polar motion excitation. *Geophysical Research Letters*, 28(12), 2457–2460. https://doi.org/10.1029/2000gl012234
- Umlauf, L., & Burchard, H. (2003). A generic length-scale equation for geophysical turbulence models. *Journal of Marine Research*, 61(2), 235–265. https://doi.org/10.1357/002224003322005087
- Wunsch, C. (1975). Internal tides in the ocean. Reviews of Geophysics, 13(1), 167–182. https://doi.org/10.1029/rg013i001p00167
- Yu, X., Ponte, A. L., Elipot, S., Menemenlis, D., Zaron, E. D., & Abernathey, R. (2019). Surface kinetic energy distributions in the global oceans from a high-resolution numerical model and surface drifter observations. *Geophysical Research Letters*, 46(16), 9757–9766. https://doi.org/10.1029/2019gl083074

MOMENI ET AL. 23 of 23